

Contract No:

This document was prepared in conjunction with work accomplished under Contract No. DE-AC09-08SR22470 with the U.S. Department of Energy.

Disclaimer:

This work was prepared under an agreement with and funded by the U.S. Government. Neither the U. S. Government or its employees, nor any of its contractors, subcontractors or their employees, makes any express or implied: 1. warranty or assumes any legal liability for the accuracy, completeness, or for the use or results of such use of any information, product, or process disclosed; or 2. representation that such use or results of such use would not infringe privately owned rights; or 3. endorsement or recommendation of any specifically identified commercial product, process, or service. Any views and opinions of authors expressed in this work do not necessarily state or reflect those of the United States Government, or its contractors, or subcontractors.

The Simulation of the Southern Great Plains Nocturnal Boundary Layer and the Low-Level Jet
with a High-Resolution Meso-Scale Atmospheric Model

David Werth¹, Monique Leclerc², Henrique Duarte², Matthew Parker¹, Nelson Luís Dias³,
Gengsheng Zhang², Marc Fischer⁴, and Robert Kurzeja¹

Corresponding author: David Werth, Savannah River National Laboratory,
david.werth@srnl.doe.gov

¹ Savannah River National Laboratory, Aiken, SC 29808

² Laboratory for Environmental physics, University of Georgia, Griffin, GA 30223

³ Universidade Federal do Parana, Centro Politecnico da UFPR Caixa, Brazil

⁴ Atmospheric Sciences Department, Lawrence Berkeley National Laboratory, Berkeley, CA 94720

Abstract

A field project over the Atmospheric Radiation Measurement-Clouds and Radiation Testbed (ARM-CART) site during a period of several nights in September, 2007 was conducted to explore the evolution of the low-level jet (LLJ). Data was collected from in situ (a multilevel tower) and remote (sodar) sensors, and the observed LLJ activity during the project was found to agree well with data from earlier studies regarding jet speed, height, and direction. To study nocturnal boundary layer (NBL) behavior, the Regional Atmospheric Modeling System (RAMS) was used to simulate the ARM-CART NBL field experiment and validated against the data collected from the site. This model was run at high resolution for calculating the interactions among the various motions within the boundary layer and their influence on the surface.

The model reproduces the changing synoptic situation as a high pressure system moves off and an arriving low produces warm, southerly advection. The simulation also produced smaller-scale convective and shear-driven eddies within the boundary layer. By adjusting the turbulence schemes properly, the model reproduces adequately the formation and dissolution cycles of the low-level jets.

1. Introduction

The stable nocturnal boundary layer (NBL) is characterized by a strong inversion and weak turbulence. It is during this time that low-level jets (LLJs) often form as a result of the decoupling between the surface conditions and the rest of the atmosphere (Bonner, 1968; Bonner and Paegle, 1970). This decoupling leads to the creation of supergeostrophic winds with flows approaching $15\text{-}25\text{ ms}^{-1}$ at levels below 1000m in the region characterized as the “Great Plains” region of the United States (Bonner, 1968; Jiang et al., 2007). During the daytime, turbulent mixing quickly damps such organized motion, but at night the surface cooling establishes an inversion which reduces turbulence and allows jets to form uninhibited.

The LLJ is an important characteristic of the southerly Great Plains boundary layer (generally below 1000m), where formation is common during the period from April to September (Jiang et al., 2007). The role of the LLJ in moisture transport and low-level convergence makes it a key factor in regional precipitation patterns (Bonner, 1968). Jiang et al. (2007) used a general circulation model (GCM) to demonstrate that the formation of the LLJ is related to both a diurnal oscillation of the pressure gradient force (associated with the greater heating and cooling of the sloping terrain) and the nocturnal damping of turbulence. Interestingly, the characterization of the Great Plains LLJ is important if that area is to be tapped as a source of wind energy, but few examples of mesoscale modeling of the LLJ and subsequent validations exist in the literature (Banta et al., 2008). Storm et al. (2009) simulated a Texas and Kansas LLJ with a 4km-resolution WRF model grid. Overall the model did well, but in both cases the simulated jet core was too high and too weak. This was attributed to problems with the parameterization of vertical mixing. The use of a mesoscale model (Zhong et al., 1996) has also been used to evaluate the proposed LLJ development mechanisms, and the simulation

reproduced several features of the LLJ; the periodicity in wind speed and direction, the level of formation, and the damping of turbulence kinetic energy (TKE) during the active LLJ periods. Cuxart et al. (2007) used a mesoscale model to study nocturnal flows on a midlatitude island, and noted how topographic features influence the stable-layer flows in the absence of strong synoptic forcing. In the simulations by Zhong et al. (1996), frictional decoupling was found to be more important than the pressure oscillation. That study, along with that of McCorcle (1988), also found soil moisture to be important, with drier soil allowing stronger jets to form.

On a finer scale, Conangla and Cuxart (2006) used a 1-D TKE model to simulate the formation of the LLJ over Spain as observed during the SABLES field project, and they noted the strong shear and large turbulence in the area above the LLJ, where thermal damping is weaker. The same project was later simulated with a large-eddy simulation (LES), set to run at 6m x 4m resolution (Cuxart and Jimenez, 2007), and the authors again noted the shear and turbulent characteristics of the above and below jet regimes.

Despite its relative stability, the NBL is characterized by turbulence across a range of scales and the turbulence is strongly related to the strength and height of the LLJ (Banta et al., 2003; Prabha et al., 2007; Smedman et al., 2004). The presence of the LLJ modulates the spectrum of motions present within the boundary layer (Conangla and Cuxart, 2006; Cuxart and Jimenez, 2007). Below the LLJ, the turbulent production (caused by the shear) is damped by buoyant motions, but immediately above the LLJ, where the shear is also strong but the stability is weaker, turbulent eddies are produced more easily. These eddies can move below the LLJ into the stable boundary layer, but the LLJ can affect this process preferentially on eddies of different sizes ---- the Smedman mechanism (i.e. the shear-sheltering mechanism) (Prabha et al., 2007; Smedman et al., 2004).

In the NBL, turbulence is dominated by smaller eddies (as opposed to daytime, when larger, convective eddies are more prominent) (Beare et al., 2006). Numerical simulations of the NBL are therefore inherently more difficult as a larger share of the turbulence must be calculated by sub-grid scale parameterizations. Overcoming this problem was the goal of the GEWEX Atmospheric Boundary Layer Study (GABLS) study, in which a set of extremely high-resolution experiments was performed to compare LES results for a range of grid spacings (from 12.5m to 1m) for a 400m x 400m domain (Beare et al., 2006). The results demonstrated the benefits of these small grid sizes since much of the turbulence was being resolved explicitly. The clock time required to run these simulations was more than a month to produce a nine hour simulation (and only two participating laboratories were able to perform simulations at the 1m resolution), so the practicality of running simulations like this regularly is doubtful at this time. Can we simulate the NBL with a more modest expense of computing power, and what will the quality of the information be? The objective of the present study is to demonstrate the applicability of the model to simulate observed boundary layer motions and to examine turbulence structure and transport at scales outside the range of field measurements.

A field project conducted at Lamont, Oklahoma in September of 2007 provides a good opportunity to test such a model and see if it can indeed produce a realistic simulation of the NBL, particularly with respect to LLJ formation. The experiment was conducted over the Atmospheric Radiation Measurement-Clouds and Radiation Testbed ARM-CART site during a period of several clear, stable nights to determine how the NBL varies during its lifecycle. Data were collected from a 10m tower (providing data at three levels of 2, 5, and 10 m continuously) and a sodar (providing data up to 900m continuously). With data limited to a single location, the full spatial and temporal range of NBL behavior is difficult, if not impossible, to determine. In

such cases, however, a model can help infer spatial and temporal information of the NBL.

The present study challenges the feasibility of this by determining the performance of the model in reproducing key large-scale motions that dominate the NBL and modulating the exchange processes at the surface. The goal is to use the model in a prognostic/deterministic mode to help experimentalists better plan their field campaigns and better interpret their boundary-layer data. (This is especially true for surface flux data.) The Regional Atmospheric Modeling System (RAMS, Pielke et al. 1992) is used to simulate the period from the field project and the model data compared to the field data collected at Lamont. The focus of this paper is on the simulation of both the diurnal LLJ lifecycle and the eddy motions (turbulence) that occur within the NBL.

2. Field Experiment

The ARM-CART site is located in Lamont, Oklahoma at 36.616N, 97.5W and was the site of the field experiment during the period from September 10, 2007 to September 24, 2007. Data were collected using three eddy-covariance flux systems using omnidirectional fast-response sonic anemometers/thermometers (Campbell Scient. Inc., Logan, UT) co-located with fast-response open-path CO₂/H₂O analyzers (Li-Cor, Lincoln, NE) placed at 2, 5, and 10m. The three velocity components (u,v,w), the virtual temperature (Ts), CO₂ concentrations and H₂O concentrations were stored with a datalogger (CR-5000, Campbell Scient. Inc., Logan, UT), all at 20Hz. Thirty-minute averages were calculated online by the datalogger, where diagnostic variables from the sonics and gas analyzers were used to filter bad data. A boundary-layer sodar (PA2, Remtech Inc., Paris, France) was also used to collect continuous 3-dimensional wind profiles up to 900m throughout the intensive observation period (IOP). The sodar data

processing unit works with an internal quality-control algorithm that rejects problematic data due to intense background noise and other adverse environmental factors. Additional wind and temperature data from the ARM-CART site was collected at 60m and by other permanent meteorological monitoring assets.

Figures 1 to 3 present histograms of height, speed, and direction of the observed low-level jets during the field campaign, and Figure 4 shows a histogram for the local time of occurrence (CDT) of the jet events. Data were compiled from 30-minute average wind speed profiles, where the LLJs were defined as the first maximum close to the surface such that the difference of wind speed at the peak and at the next higher minimum was larger than 2 ms^{-1} (the same threshold used by Andreas et al. (2000)).

The typical LLJ height observed during the campaign (Fig.1) was between 225 and 360 m AGL, similar to the results obtained by Whiteman et al. (1997) using data collected at the same location, showing a frequency peak in the 200-400m AGL range. Figure 2 shows that the LLJ speed of $\sim 12\text{-}14 \text{ ms}^{-1}$ was most frequent during the campaign, but relatively high frequencies were also observed for winds, up to $\sim 23 \text{ ms}^{-1}$. Whiteman et al., (1997) reported typical jet speeds of $15 \text{ to } 21 \text{ ms}^{-1}$ for their study.

Figure 3 shows a clear predominance of southerly jets, in agreement with other studies of the Great Plains LLJ (e.g. Bonner, 1968; Whiteman et al., 1997). The frequencies observed for the directions between 330 and 120 (NNW – ESE) correspond to the first days of the campaign (before Sept. 15th, 12:30 CDT), when the jets were caused by a different synoptic-scale phenomenon. According to Whiteman et al., (1997), northerly jets at the Great Plains are generally related to southward-moving cold fronts, while the southerly jets seen during the present campaign were induced by southerly flows ahead of cold fronts advancing from the west.

Figure 4 illustrates that the LLJ is not an exclusively nocturnal phenomenon, as already reported by Bonner (1968). The lowest frequencies are found between 11:00 and 19:00 hrs (CDT). Bonner (1968), based on observations at 00:00, 06:00, 12:00, and 18:00 (CST), found lower frequencies for 12:00 and 18:00 hrs and higher and similar frequencies for 00:00 and 06:00 hrs, similar to the results obtained in this study. Whiteman et al., (1997) also reported a lower frequency of occurrence for soundings at 11:00, 14:00 and 17:00 CST during the warm season, and higher frequencies at 02:00, 05:00, 08:00, 20:00, and 23:00 CST.

Figures 5, 6, and 7 present the observed jet height, speed, and direction as a function of time during the RAMS simulation period (September 14th, 18:00 CST to September 17th, 18:00 CST). For the nights in Fig. 7, it can be seen that the jets undergo an inertial oscillation (note the clockwise turning of the jets, i.e. a positive change in jet direction) over time for each night. The jets start from a minimum speed and height at approximately 21:00 CDT and reach a maximum speed and height around 09:00 CDT.

3. Boundary Layer Simulation with RAMS

a. The Model

The Regional Atmospheric Modeling System (Pielke et al., 1992) was used to simulate the nocturnal boundary layer for this experiment. RAMS can be run at high resolution and is ideal for calculating the interactions among the various motions within the boundary layer and their influence on the surface (Buckley and Kurzeja, 1997; Avissar et al., 1998; Gopalakrishnan and Avissar, 2000). The model solves the non-hydrostatic equations of motion for velocity and potential temperature on a staggered C-grid (Arakawa and Lamb, 1977) with a polar-stereographic projection. A terrain-following sigma coordinate system, in which the bottom of

the model domain follows the terrain, exists in the vertical direction. The Harrington radiative transfer scheme (Gabriel et al., 1998), which uses a two-stream approximation, is applied to both longwave and shortwave radiation. The Kuo cumulus scheme (Kuo, 1974), in which moisture convergence is converted to convective motion, was selected as the cumulus parameterization for the coarser grids (Grids 1 and 2). For the finer grids, a cloud prognostic scheme (Cotton et al., 1986; Meyers et al., 1992) was used. For the surface scheme, which plays a large role in determining model surface fluxes, the LEAF-3 surface scheme was used (Walko et al., 2000). Each grid square is assigned a fraction of 21 land surface types (based on USGS 1km AVHRR data), and each type is assigned its own set of variables (leaf area index, albedo, etc.). The fluxes are calculated for each type individually, and then averaged to determine the grid-averaged fluxes. Other surface data include 30 second topography, and 1 kilometer FAO soil type data.

Within the atmosphere, unresolved eddy transport is accomplished with K-theory. The method used to determine the value of the eddy diffusivity (K) is dependent on the eddy-diffusion scheme selected. For all five grids, horizontal diffusion is calculated using the product of the horizontal deformation rate, the grid spacing, and a user-set parameter, set to 0.32. This scheme also requires the user to set a ratio of scalar-to-velocity diffusion (set to 3.0 in our simulations), and a minimum value of horizontal diffusion is set to 0.1 for Grids 1-4 and 0.75 for Grid 5. These values were set to allow for a relatively weak parameterized turbulent diffusion, which allows for more resolved turbulent activity to develop in the model. The Mellor-Yamada scheme (applied as in Mellor-Yamada, (1974)) is used to calculate K for vertical diffusion, using a prognostic TKE. This prescription produces relatively weak diffusion in the inner 2 domains. We will see that while this can result in some noise to turn up in the simulation, it also allows for sharper gradient to persist and smaller-scale features to develop.

As the model simulates atmospheric conditions, a simple Newtonian relaxation scheme is applied to nudge the outermost grid (Grid 1) towards the predetermined boundary values, while the inner grids are each relaxed towards the boundary values from their respective parent grids in a similar way. The relaxation is applied most strongly at the outermost edge, and the strength gradually decreases to zero within 5 gridpoints of the boundary. In this way, each grid is constrained near the boundary but is freer to produce small-scale motions in the interior. Two-way nesting is also applied, so each parent grid is influenced by its respective interior grid (Clark and Hall, 1991).

b. Application of RAMS

RAMS simulated the period from Sept. 15th 0000UTC (Sept. 14th, 7:00pm, all times are Central Daylight Time) to 0006UTC (1:00am) Sept. 18th, 2007, with a domain centered over the ARM-CART site in Lamont, OK (36.616N, 97.5W). This period was selected as it was concurrent with a large number of observational data at that site, and several LLJs were observed on these nights. It is also a period of steadily changing synoptic pattern, with different jet characteristics for each night (Fig. 6,7). The field data collected during the field experiment serves as the standard for validating the model.

A series of 5 nested grids, with horizontal grid spacing of 32km (52x52), 8km (54x54), 2km (74x74), 500m (150x150), and 125m (50x50) (Fig. 8) were used. The plot shows the south-central US, with terrain rising to the west, a key component of LLJ formation. The two innermost grids encompass areas of relatively little topographic relief (Fig. 8b). The outermost grid is forced by 81km data from the Rapid Update Cycle model (Benjamin, 2004), with an update period of 6 hours. The vertical spacing for all grids is 30m at the surface, exponentially

expanding by 15% per layer to a maximum of 1000m above 8000m, and the model extends up to 12.8km. In this way, fine-scale motions near the surface can be resolved while allowing for a coarser (and less computationally expensive) vertical resolution aloft, where such motions are less relevant. The time step is 60 seconds for the outermost grid, reduced to 0.833 seconds for the finest grid.

To initialize the soil conditions, a series of lower resolution runs was done (with Grids 1-3 only), each starting at Sept. 12 at 0000UTC and running for six days, ending at Sept. 18th at 0006UTC. These runs were each initialized with different values of soil wetness and total soil energy, and the one that produced the best low-resolution forecast (determined by comparing the 2m and 60m temperatures and winds at the field project site to the observed values) for the period in question (Sept. 15th - Sept. 18th) was selected to be run for the same period at the higher-resolution (Grids 1-5). The result suggested that the best way to run the model was to start it with very high values of soil energy ($2.18 \times 10^8 \text{ J/m}^3$), and fairly high values of soil wetness (0.235, about half-way to saturation). During the three-day spin-up, the model had the opportunity to ‘dump’ the excessive heat and moisture, with the result being smaller, more realistic values of soil moisture and energy by Sept. 15th at 0000UTC, producing a more accurate higher-resolution simulation of the subsequent three-day period.

A subsequent nocturnal simulation was performed with an even finer spatial (6th) grid of 32.5m horizontal resolution for Sept. 17th from 0800UTC-1330UTC (a period characterized by surface cooling and stability). The vertical spacing was also enhanced to increase the number of vertical levels within the boundary layer. Theoretically, more turbulence should now be explicitly resolved, allowing for a lower amount of parameterized sub-grid scale turbulent diffusion (Zhong and Fast, 2003). Therefore, we now apply the turbulent diffusion scheme of

Deardorff (1980), which uses a prognostic TKE scheme to determine the K-values. This scheme results in weaker turbulent diffusion, again allowing for the production of smaller-scale eddies.

4. Results

a. Synoptic Conditions

During the period of the model simulations, the Midwest was dominated by a high pressure system that gradually moved east (Fig. 9), with the associated southerly winds and warm advection on its west side over the Plains. At 0000UTC on the 15th, NCEP reanalysis data (Kalnay et al., 1996) show that in northern Oklahoma (Fig. 10a), winds are from the north-northeast, and the temperature is in the low 20s. Grid 1 simulation data compares well to that time (Fig. 10b). The next evening, southeasterly winds develop as the high moves to the east (Fig. 10c). The model winds shift more southerly (Fig. 10d), and the model temperature is close to the observed temperature. On the evening of the 16th, the cold front moves closer, and southerly winds bring warm air to the area. The model winds and temperatures are similar (Figs. 10e,f). Near the end of the period, a low pressure system moved to the north and generated a line of thunderstorms over Minnesota, Kansas and Nebraska (Fig. 9).

As an additional synoptic-scale validation, a time series of 2m temperature and 10m wind speed was created over three Great Plains stations - Hays, KS, Hastings, NE, and Abilene, TX (see Fig. 8 for locations). Grid 1 data from these same locations was extracted from the model results, and the time series are compared in Fig. 11. The model generally does well, capturing the diurnal cycle and the different multi-day trends, although some details are missed. For example, it is slightly too warm over Nebraska and over Kansas at night, and slightly too cool over daytime Kansas and Texas. The model winds (Fig. 11) also capture the synoptic-scale

trends, though some higher-frequency variability is missed.

The conditions that prevail over the period – strong synoptic forcing with southerly flow – are conducive to the formation of a nocturnal low-level jet as radiant cooling of the surface (due to clear skies) increases stability and reduces the drag that turbulent motions tend to exert on winds at the top of the boundary layer. This can be seen more clearly by examining the model boundary layer and comparing it to the ARM-CART data from that time.

b. Evolution of the Nocturnal Boundary Layer

The Grid 5 domain (125m) should be able to resolve smaller-scale features in the boundary layer. To verify that the Grid 5 domain is producing small-scale spatial variability, the wind speed at 296m is plotted in Fig. 12 for three nocturnal and three daytime periods. (To concentrate on the part of the domain least influenced by the boundary, only the inner 4km x 4km part of the domain is shown.) The plots do show some noise, a consequence of the low model diffusion, but also show that the weaker diffusion allows for small-scale features with strong gradients to develop, particularly during the day. The model NBL is characterized by weaker gradients and smaller intra-domain differences than the more active daytime boundary layer, which is dominated by rolls and other convective patterns, but we can conclude from these that the model is capable of producing and resolving eddy activity.

To explore the NBL in more detail, data from Grid 5 is compared to actual data from the field campaign with a focus on the formation and dissipation of the LLJ. The model data at the field site is compared to the SODAR readings (both are at 30 minute intervals), which provide wind speed and direction up to 900m. On the night of the 14th and into the early morning on the 15th (Fig. 13) the simulated LLJ forms slightly early (at about 0600UTC, compared to 0900UTC

for the sodar, likely due to inadequate vertical mixing), but at essentially the correct level (300-400m). The LLJ dissipates at around 1400UTC on the 15th in both the observation and the model. On the night of the 15th, the downward propagation of the LLJ in both observations and the model is evident, though the model LLJ fails to intensify as it reaches its lowest level (200m) or develop a distinct core. The model winds at 900m also appear slightly too strong as compared to SODAR data. The model shows the shift of wind direction from easterly to southeasterly, but some discrepancies exist. For example, the model fails to capture the turbulent winds at 2000UTC to 0000UTC at 100 to 500m (again, weak vertical mixing by the model during the afternoon could be the problem).

On Sept. 16th (Fig. 14), the modeled LLJ again initiates slightly early (0700UTC), and reaches its maximum intensity earlier (at 1200UTC, compared to 1500UTC in the observations). The modeled LLJ is stronger than the observed, but forms at about the right height (500m), and dissipates on the 16th at the correct time as well (by about 1700UTC). The LLJ reforms at 0100UTC the next night, reaching an appropriate intensity but forms a little higher in the model (at 500m, compared to 300m in the observations). The jet-level wind arrows indicate that the observed shift from southwesterly to southerly occurs in the model as well.

On Sept. 17th (Fig. 15), the LLJ forms shortly after midnight (0005UTC), and the core lies at 350m. The model LLJ starts and ends at the correct times, but forms higher at about 600m, and is probably too strong. Like the LLJ of the 17th, the LLJ of the 18th occupies a deep layer (though partially obscured above 400m by missing data in the SODAR). The model LLJ has this characteristic as well, but does not develop a distinct core at 200-300m as seen in the SODAR. (In most modeled cases, the jet seems to extend too high, occupying a deeper layer of the atmosphere than observed. This is likely due to inadequate vertical mixing in the M-Y scheme.)

The wind arrows show how the model captures the southwesterly winds shifting to southeasterly at 200-500m, but does not capture the stronger southeasterly component above this layer.

Ultimately, the meteorological conditions aloft are linked to conditions at the surface. At 5m, for example, RAMS data are too warm on the first day (Fig. 16a), though more accurate the other days. This is likely due to inadequate cloud modeling, as surface radiative fluxes are higher than observed (not shown). At 60m (Fig. 16c), we see the daytime highs are reasonably accurate, but the nighttime lows are cooler, especially on the first and third nights. The model tracks well the diurnal cycle in wind activity at 5m and 60m (Fig. 16b,d), but the nocturnal 5m winds are too strong the first two nights, and the 60m daytime winds are too slow on the first day.

A comparison of the surface fluxes (Fig. 17a,c) shows that the model fluxes are reasonably accurate, with some variations from the observed data. The daytime sensible heat fluxes are too high, but the model does not capture the large latent fluxes on the second and third days. The model water vapor (Fig. 17b) is very close to the observations during most of the simulation times, suggesting that the model evapotranspiration (which represents a strong control on the surface heat transfer and the consequent turbulent mixing) is accurate, though errors do exist. The 5m values of u^* are also compared as a measure of turbulent momentum flux (Fig. 17d), and while the model does well overall, it seems to have too much momentum transport, especially at night.

On synoptic scales, the model does well, capturing the temperature changes and backing wind associated with the departing high pressure system. On the scale of the boundary layer, the model can simulate the cycle of LLJ formation and dissipation, though occasional differences exist in the details of intensity, timing and location. Many of the turbulent motions that characterize the boundary layer, however, cannot be resolved reliably with the 125m resolution

of Grid 5. If we wish to study these motions, we must go to a finer scale.

c. Study of the Turbulent Scales

The high-resolution (grid spacing = 32.5m) simulation was performed to capture better the model behavior during the periods of maximum atmospheric stability (between the black arrows on Fig. 15, top). At that time, the jet is strongest, and will therefore exert its strongest effect on the model eddy dynamics. A model sounding from 12UTC (Fig. 18a) clearly shows the nocturnal temperature lid at 925mb. It is above this point that the jet reaches its maximum speed and the ‘nose’ develops. Above about 900mb, we see the jet weakening as temperatures fall with height and thermal stability is no longer exerting a damping effect on the production of eddy motion through shear. A comparison with the observed sounding (Fig. 18b) from that time reveals the capping inversion, but the model is too warm, and does not capture the inversion above 850mb (possibly a subsidence inversion at the poorly-resolved higher levels) or the corresponding sharp rise in wind speed above 800mb. Also, the model does not show the shallow inversion near the surface seen in the observations, likely due to a model failure to radiate heat at night.

We may suppose that the NBL is characterized by weak turbulence until sunrise initiates surface heating. Turbulence is damped when the Richardson number exceeds 0.25, and this does not occur in the vertical until about 250m aloft for most sampled model times (Fig. 18c). Some turbulent motions may exist below this level, while the damping of motions above this level is likely (thereby insulating the LLJ).

Figure 19a shows the 60m model wind speed from Grid 6 of the 6-grid run, along with the difference between the Grid 5 and Grid 6 60m wind speed. It can be seen that grid 6 contains

higher frequency components than grid 5, as expected, but at very low amplitudes, i.e., less than 0.1 m/sec. The difference between RAMS and observations is also apparent in the comparison between the RAMS 60 m wind speed for a 5-hour period at night with the corresponding ARM tower values (Fig.18b). The observed data show mixed long and short period frequencies. Specifically, wind observations exhibit slow modes of low-amplitude variability, with superimposed turbulent modes, with amplitudes of ~ 1 m/s, which is an order of magnitude larger than the 0.1 m/s amplitudes in the model. The model wind speed shows much weaker long-period variability - the observed data varies over a much greater range at all timescales (covering a range from $6-14\text{ms}^{-1}$, compared to $10.3-10.6\text{ms}^{-1}$ in the model).

The power spectrum of the wind speed time series can reveal more about the timescales on which both the model and the observations vary. The spectra for both the model and the observation time series seen in Fig. 19b are calculated. For the observational time series, the larger variability means that nonstationarity can distort the power spectra. Therefore, the observed time series is first divided into four 256-point series (using only the first 1024 points), and the spectrum calculated for each. The four spectra are then averaged to get a single, representative spectrum. (For the model time series, the 1-minute data means that the entire 5.5 hour series is little longer than 256 points, so only a single spectrum is calculated.) All four spectra are then bin-averaged (using 44 bins, each with an equal frequency range) to further smooth out the noise in the spectra, and the results are seen in Fig. 19c.

The model spectrum exhibits between one and two orders of magnitude less power than the observed spectra at all frequencies. However, the model spectrum exhibits the $-5/3$ decrease with frequency characteristic of the inertial subrange at all frequencies, while the observations show this behavior only at higher frequencies. The observed spectra is similar to the results of

Caughey (1982) for the stable boundary layer, who noted that the spectral gap (at ~ 0.008 Hz) separates low frequency wave activity from turbulence in the inertial subrange.

The absence of the local high frequency spectral maximum in the model suggests that the turbulent energy at 60m in the model is not surface-generated but rather transported downward from the jet. Furthermore, the model energy deficit at lower frequencies suggests either insufficient in-situ turbulence generation (e.g., by gravity waves) or insufficient transmission of turbulence/ wave energy downward from the jet. Model wind speeds at 3 elevations above the site can be seen in Fig. 20, and the turbulent kinetic energy calculated from these using 30 minute intervals for the 5-hour period was found to decrease from about $0.17 \text{ m}^2/\text{s}^2$ at 550 m to $0.01 \text{ m}^2/\text{s}^2$ at 50 m. These numbers contrast with values measured over $\frac{1}{2}$ hour periods by the Doppler sodar of $\sim 4 \text{ m}^2/\text{s}^2$ at the jet maximum and $1 \text{ m}^2/\text{s}^2$ at 60 meters. The sodar-derived value at 60m is consistent with the tower measurements (Fig. 19b). The model data also contrast with Banta et al., (2003) who found TKE values of $0.5 - 1.0 \text{ m}^2/\text{s}^2$ at 60 m, though the model TKE agrees better with their data at the jet maximum, where they calculated 0.1 to $0.5 \text{ m}^2/\text{s}^2$ at the jet maximum for 10 minute averages. Thus, we conclude that the model turbulent kinetic energy is approximately one order of magnitude less than observations at all elevations. Moreover, since much of the turbulence created by wind shear at the jet, the deficit cannot be attributed solely to poor resolution of surface features.

Figure 19 shows that the high-resolution model cannot capture the full variability observed at the shorter time scales. The spectrum does show, however, that some variability does exist at all resolved scales, and that the model turbulence does follow an expected distribution, implying that the simulated interaction between eddies (and the consequent cascade from large to small scales) is occurring in a realistic way. Therefore, the model variability that does exist can still be

used to tell us about nocturnal boundary layer turbulence.

To examine modeled NBL activity, we apply a wavelet analysis to the time series (Torrence and Compo, 1998). The use of wavelets allows the user to analyze a time series into its timescale components, but is continuously applied to a subset of the data that shifts in time. It is similar to a Fourier analysis, with the added feature that the analysis is localized in time, allowing for intense but short-lived events to appear in the resulting spectrum without being reduced by averaging. Wavelet analysis has proven very useful in the analysis of boundary layer motions (Cuxart et al., 2002; Terradellas et al., 2005; Prabha et al. 2008), as it can identify modes of variability that persist for short periods, and nonstationarity is another prominent characteristic of the NBL. We elect to use a Morlet wavelet of order 6 (Prabha et al., 2007), which has been applied to NBL time series analysis before and proven itself useful in identifying events at various timescales.

We select the model wind speed at 279m as the time series to analyze. The linear trend (which can be misinterpreted as a long-period oscillation) is removed, and a time-filter is applied to examine separately the effects on turbulent and slowly-varying motions. A 30-minute running average is applied to the time series of wind speed at several levels to get the low-frequency (LF) component, and the LF series is then subtracted from the original time series to get the high-frequency (HF) component. The LF component (Fig. 21a) is dominated by eddies of 128 minute period, persisting throughout the simulation. The HF component (Fig. 21b) has a broader spectrum, with most of its activity between 15 and 30 minutes during the first 3.0 hours, with less intense peaks at 38 and 128 minutes. The wavelets also reveal the general homogeneity of the low frequencies in the boundary layer, with spectra at 2m and 164m (not shown) similar to that at 279m for the LF components. For the HF components, the peak periods gets shorter as

one rises from 2m (53 minutes, not shown) to 279m (19 minutes, Fig. 21b), suggesting again that the jet is a source of high-frequency variability.

5. Conclusions

A numerical mesoscale model, RAMS, can accurately simulate the behavior of the nocturnal boundary layer including its formation and eventual dissipation. While mean temperature and winds were simulated reasonably well by the model, the model turbulence and wave energy were less than observed, implying that it had difficulty converting the strong shear in the resolved flows into resolved and parameterized turbulent motion. The modeled high frequency variability was lower than observations indicated, but many of the relevant motions within the boundary layer could still be discerned by adjusting the turbulence scheme to reduce sub-grid turbulent diffusion and force the resolved motions to perform the eddy diffusion. The results thus support the general observation of Banta et al. (2003) that the detailed surface structure may play a minor role in the evolution of the jet and mean structure of the boundary layer.

There are benefits that can be derived from accurate modeling of the NBL. First, the model can be used to elucidate atmospheric boundary layer behavior in a particular location. More so than existing analysis data (such as the NCEP reanalysis), the model can provide guidance on NBL features such as the strength of the LLJ and the timing of its formation. Details such as these can be useful in interpreting the results from field experiments and long-term monitoring projects. This is important as the NBL may be particularly sensitive to changes in radiative forcing (Cava et al., 2004; Walters et al., 2007), so its behavior can vary greatly even during periods of seemingly unvarying larger-scale forcing. Future model enhancements will

focus on high-frequency nocturnal variability and the data gap filling process (Baldocchi, 2008).

Acknowledgements

Prepared for the U.S. Department of Energy Under Contract Number DE-AC09-08SR22470.

This work was sponsored by the DOE Office of Science – Terrestrial Carbon Processes Program (Contract #ER64321-1028996-0012858 for the University of Georgia). Select data were obtained from the Atmospheric Radiation Measurement (ARM) Program sponsored by the U.S. Department of Energy, Office of Science, Office of Biological and Environmental Research, Environmental Sciences Division.

References

Andreas, E.L., K.J. Claffey, and A.P. Makshtas, 2000. Low-level atmospheric jets and inversions over the Western Weddell Sea. *Boundary-Layer Meteorology* 97, 459—486.

Arakawa, A. and R. V. Lamb, 1977: *Computational design of the basic dynamical processes of the UCLA general circulation model*. Vol. 17, *Methods in Computational Physics*, Academic Press, pp. 173-265

Avissar, R., E.W. Eloranta, K. Güreş, and G.J. Tripoli, 1998: An Evaluation of the Large-Eddy Simulation Option of the Regional Atmospheric Modeling System in Simulating a Convective Boundary Layer: A FIFE Case Study. *J. Atmos. Sci.*, **55**, 1109–1130.

Baldocchi, D., 2008: 'Breathing' of the terrestrial biosphere: lessons learned from a global network of carbon dioxide flux measurement systems, *Aus. Jour. Bot.*, **56**, 1-26.

Banta, R.M., Y.L. Pichugina, and R.K. Newsom, 2003: Relationship between Low-Level Jet Properties and Turbulence Kinetic Energy in the Nocturnal Stable Boundary Layer. *J. Atmos. Sci.*, **60**, 2549–2555.

Banta, R., Y. Pichugina, N. Kelley, and W. Brewer, 2008: Characterizing the Great Plains Low-Level Jet Wind Resource using Doppler Lidar, AGU Fall Meeting, San Francisco, CA

Beare, R., M. MacVean, A. Holtslag, J. Cuxart, I. Esau, J-C. Golaz, M. Jimenez, M. Khairoutdinov, B. Kosovic, D. Lewellen, T. Lund, J. Lundquist, A. McCabe, A. Moene, Y. Noh, S. Raasch, and P. Sullivan, (2006), "An Intercomparison of Large-Eddy Simulations of the Stable Boundary Layer", *Bound.-Layer Meteor.*, **118**, 247-272.

Benjamin, S.G., D. Dévényi, S.S. Weygandt, K.J. Brundage, J.M. Brown, G.A. Grell, D. Kim, B.E. Schwartz, T.G. Smirnova, T.L. Smith, and G.S. Manikin, 2004: An Hourly Assimilation–Forecast Cycle: The RUC. *Mon. Wea. Rev.*, **132**, 495–518.

Bonner, W.D., 1968: Climatology of the Low level Jet. *Mon. Wea. Rev.*, **96**, 833–850.

Bonner, W.D., and J. Paegle, 1970: Diurnal Variations in Boundary Layer Winds over the South-Central United States in Summer. *Mon. Wea. Rev.*, **98**, 735–744.

Buckley, R.L., and R.J. Kurzeja, 1997: An Observational and Numerical Study of the Nocturnal Sea Breeze. Part I: Structure and Circulation. *J. Appl. Meteor.*, **36**, 1577–1598.

Caughey, S.J., 1982. The observed characteristics of the atmospheric boundary layer. in *Atmospheric Turbulence and Air Pollution Modeling*, Ed. F.T.M. Nieuwstadt and H. van Dop. D. Reidel, Dordrecht, Holland.

Cava, D., U. Giostra, M. Siqueira and G. Katul, 2004: Organised Motion and Radiative Perturbations in the Nocturnal Canopy Sublayer above an Even-Aged Pine Forest, *Bound.- Layer Meteor.*, **112**, 129-157.

Clark, T.L., and W.D. Hall, 1991. Multi-domain simulations of the time dependent Navier-Stokes equations: Benchmark error analysis of some nesting procedures. *J. Comput. Phys.*, **92**, 456-481.

Conangla, L., and J. Cuxart, 2006: On the Turbulence in the Upper Part of the Low-Level Jet: An Experimental and Numerical Study, *Boundary-Layer Meteorology*, **118**, Issue 2, pp.379-400

Cotton, W. R., Tripoli, G. J., Rauber, R. M., Mulvihill, E. A., 1986: Numerical simulation of the effects of varying ice crystal nucleation rates and aggregation processes on orographic snowfall. *J. Climate Appl. Meteor.*, **25**, 1658-1680.

Cuxart, J., G. Morales, E. Terradellas, and C. Yague, 2002 : Study of Coherent Structures and Estimation of the Pressure Transport Terms for the Nocturnal Stable Boundary Layer, *Boundary-Layer Meteorology*, **105**, 305-328

Cuxart, J., and M.A. Jiménez, 2007: Mixing Processes in a Nocturnal Low-Level Jet: An LES Study. *J. Atmos. Sci.*, **64**, 1666–1679.

Cuxart, J., M.A. Jiménez, and D. Martínez, 2007: Nocturnal Meso-Beta Basin and Katabatic Flows on a Midlatitude Island. *Mon. Wea. Rev.*, **135**, 918–932.

Deardorff, J., 1980: Stratocumulus-capped mixed layers derived from a three-dimensional model, *Bound. Lay. Met.*, **18**, 495-527

Gabriel, P., J. Harrington, G. Stephens, and T. Schneider, 1998: Adjoint Perturbation Method Applied to Two-Stream Radiative Transfer, *J. Quant. Spectrosc. Radiat. Transfer*, **59**, 1-24.

Gopalakrishnan, S.G., and R. Avissar, 2000: An LES Study of the Impacts of Land Surface Heterogeneity on Dispersion in the Convective Boundary Layer. *J. Atmos. Sci.*, **57**, 352–371.

Jiang, X., N.-C. Lau, I. Held, and J. Ploshay, 2007: Mechanisms of the Great Plains Low-Level Jet as Simulated in an AGCM, *J. Atmos. Sci.*, **64**, 532-547.

Kalnay, E., M. Kanamitsu, R. Kistler, W. Collins, D. Deaven, L. Gandin, M. Iredell, S. Saha, G. White, J. Woollen, Y. Zhu, A. Leetmaa, R. Reynolds, M. Chelliah, W. Ebisuzaki, W. Higgins, J. Janowiak, K. Mo, C. Ropelewski, J. Wang, R. Jenne, and D. Joseph, 1996: The NCEP/NCAR 40-Year Reanalysis Project. *Bull. Amer. Meteor. Soc.*, **77**, 437-471.

Kuo, H., 1974: Further studies of the parameterization of the influence of cumulus convection on large-scale flow. *J. Atmos. Sci.*, **31**, 1232-1240.

McCorcle, M.D., 1988: Simulation of Surface-Moisture Effects on the Great Plains Low-Level Jet. *Mon. Wea. Rev.*, **116**, 1705-1720.

Mellor G. L., and T. Yamada, 1974: A hierarchy of closure models for planetary boundary layers, *J. Atmos. Sci.*, **31**, 1791-1806

Meyers, M. P., DeMott, P.J., Cotton, W.R., 1992: New primary ice nucleation parameterizations in an explicit cloud model. *J. Appl. Meteor.*, **31**, 708-721.

Pielke R. A., W. R. Cotton, R. L. Walko, C. J. Tremback, W. A. Lyons, L. D. Grasso, M. E. Nicholls, M. D. Moran, D. A. Wesley, T. J. Lee, and J. H. Copeland, 1992: A comprehensive meteorological modeling system--RAMS. *Meteor. Atmos. Phys.*, **49**, 69-91.

Prabha, T.V., M.Y. Leclerc, A. Karipot, and D.Y. Hollinger, 2007: Low-Frequency Effects on Eddy Covariance Fluxes under the Influence of a Low-Level Jet. *J. Appl. Meteor. Climatol.*, **46**, 338–352.

Prabha, T., M. Leclerc, A. Karipot, D. Hollinger, and E. Mursch-Radlgruber, 2008: Influence of Nocturnal Low-level Jets on Eddy –covariance Fluxes over a Tall Forest Canopy, *Bound.-Lay. Met.*, **126**, 219-236.

Smedman, A., U. Högström, and J. Hunt, 2004: Effects of shear sheltering in a stable atmospheric boundary layer with strong shear. *Quart. J. Roy. Meteorol. Soc.*, **130**, 31-50.

Storm, B., J. Dudhia, S. Basu, A. Swift, and I. Giammanco, 2009: Evaluation of the Weather Research and Forecasting Model on Forecasting Low-level Jets: Implications for Wind Energy. *Wind Energy*, **12**, 81-90.

Terradellas, E., M. Soler, E. Ferreres, and M. Bravo, 2005: Analysis of oscillations in the stable atmospheric boundary layer using wavelet methods, *Boundary Layer Met.*, **114**, 489-518

Torrence, C., and G.P. Compo, 1998: A Practical Guide to Wavelet Analysis. *Bull. Amer. Meteor. Soc.*, **79**, 61–78.

Walko, R.L., L.E. Band, J. Baron, T.G.F. Kittel, R. Lammers, T.J. Lee, D. Ojima, R.A. Pielke, C. Taylor, C. Tague, C.J. Tremback, and P.L. Vidale, 2000: Coupled Atmosphere–Biophysics–Hydrology Models for Environmental Modeling. *J. Appl. Meteor.*, **39**, 931–944.

Walters, J. T., R. T. McNider, X. Shi, W. B. Norris, and J. R. Christy, 2007: Positive surface temperature feedback in the stable nocturnal boundary layer, *Geophys. Res. Lett.*, **34**, L12709, doi:10.1029/2007GL029505.

Whiteman, C.D., X. Bian, and S. Zhong, 1997. Low-level jet climatology from enhanced rawinsonde observations at a site in the Southern Great Plains. *J. Appl. Meteorol.* **36**, 1363—1376.

Zhong, S., J. Fast, and X. Bian, 1996: A Case Study of the Great Plains Low-Level Jet Using Wind Profiler Network Data and a High-Resolution Mesoscale Model, *Mon. Wea. Rev.*, **124**, 785-806.

Zhong, S., and J. Fast, 2003: An Evaluation of the MM5, RAMS, and Meso-Eta Models at Subkilometer Resolution Using VTMX Field Campaign Data in the Salt Lake Valley. *Mon. Wea. Rev.*, **131**, 1301–1322.

Figure 1 Histogram of jet height observed during the field campaign.

Figure 2 As in Fig. 1 but for jet speed.

Figure 3 As in Fig. 1 but for jet direction.

Figure 4 As in Fig. 1 but for time of occurrence.

Figure 5 Time series of jet height during the period selected for simulation.

Figure 6 As in Fig. 5 but for jet speed.

Figure 7 As in Fig. 5 but for jet direction.

Figure 8 a) Grids 1-4 used in the RAMS simulations, along with the topography in meters.

b) As in a) but for grids 4 and 5. The black square indicates the location of the ARM central Facility, where the field project was conducted. The three black dots indicate stations (Hays, KS, Hastings, NE, and Abilene, TX) used for validation.

Fig. 9 Synoptic maps for a) 12Z, Sept. 15th, b) 12Z, Sept. 16th, c) 12Z, Sept. 17th, d) 12Z, Sept. 18th. Maps are from the NCEP, Hydrometeorological Prediction Center (<http://www.hpc.ncep.noaa.gov/dailywxmap/>).

Fig. 10 Synoptic surface temperatures ($^{\circ}\text{C}$, contours) and winds (m/s, vectors) during the period from a) NCEP Reanalysis at Sept. 15, 0Z, b) RAMS at Sept. 15, 0Z, c) NCEP Reanalysis at Sept. 16, 0Z, d) RAMS at Sept. 16, 0Z, e) NCEP Reanalysis at Sept. 17, 0Z, f) RAMS at Sept. 17, 0Z

Fig. 11 RAMS grid 1 (thick line) and observed (thin line) temperature (left) and wind speed (right) at the stations (see Fig. 8) in a) Nebraska, b) Kansas, c) Texas. Observed data is from the NCDC Climate Database (<http://cdo.ncdc.noaa.gov/pls/plclimprod/poemain.accessrouter?datasetabbv=DS3505>).

Figure 12 Horizontal wind speed (m/s) at 296m within the Grid 5 domain at a) 7Z, 9/15/07, b) 13Z, 9/16/07, c) 12Z, 9/17/07, d) 17Z, 9/15/07, e) 20Z, 9/16/07, and f) 21Z, 9/17/07.

Horizontal units are in kilometers.

Figure 13 RAMS (top) vs. SODAR (bottom) 9/15 (midnight to midnight, CDT) wind speed (m/s, colors) and direction (arrows) as a function of height (m) at the field site.

Figure 14 As in Fig. 13 but for 9/16.

Figure 15 As in Fig. 13 but for 9/17. The black arrows indicate the nocturnal period simulated by the high-resolution model.

Fig. 16 a) Temperature ($^{\circ}\text{C}$) at the tower (thin line) and in the model (thick line) at 5m, b) as in a) but for 5m wind speed, c) as in a) but for temperatures at 60m, d) as in b) but for wind speeds at 60m. Both observed and model data is at 30 minute sampling.

Fig. 17 RAMS simulated (thick line) and observed tower (thin line) a) sensible heat flux, b) water vapor, c) latent heat flux, and d) u^* . Both observed and model data is at 30 minute sampling.

Fig. 18 a) Sounding of model temperature (thick line) and wind speed (thin line) at 12Z, Sept. 17, b) As in the top plot but for the observed sounding at the site (<http://www.arm.gov/>), c) Model Richardson number at several times during the 5.5 hour simulation period.

Figure 19 a) Site 60m wind speed from the Grid 6 run (thick line, left axis), along with the difference between the grid 5 and grid 6 runs (thin line, right axis). b) Observed (thin line) and simulated (thick line) 60m wind speed at the site from the 5.5 hour high resolution run. c) Power spectra of the observed and simulated 60m windspeed. The black line follows a $-5/3$ power law.

Figure 20 a) Modeled site wind speed at 550m (thick line, left axis), 350m (thin line, left

axis), and 150m (dotted line).

Fig. 21 Wavelet analysis of the 279m field site model windspeed for the a) LF and b) HF components. All data seen are significant at the 95% confidence level. Power units are m^2/s^2 .

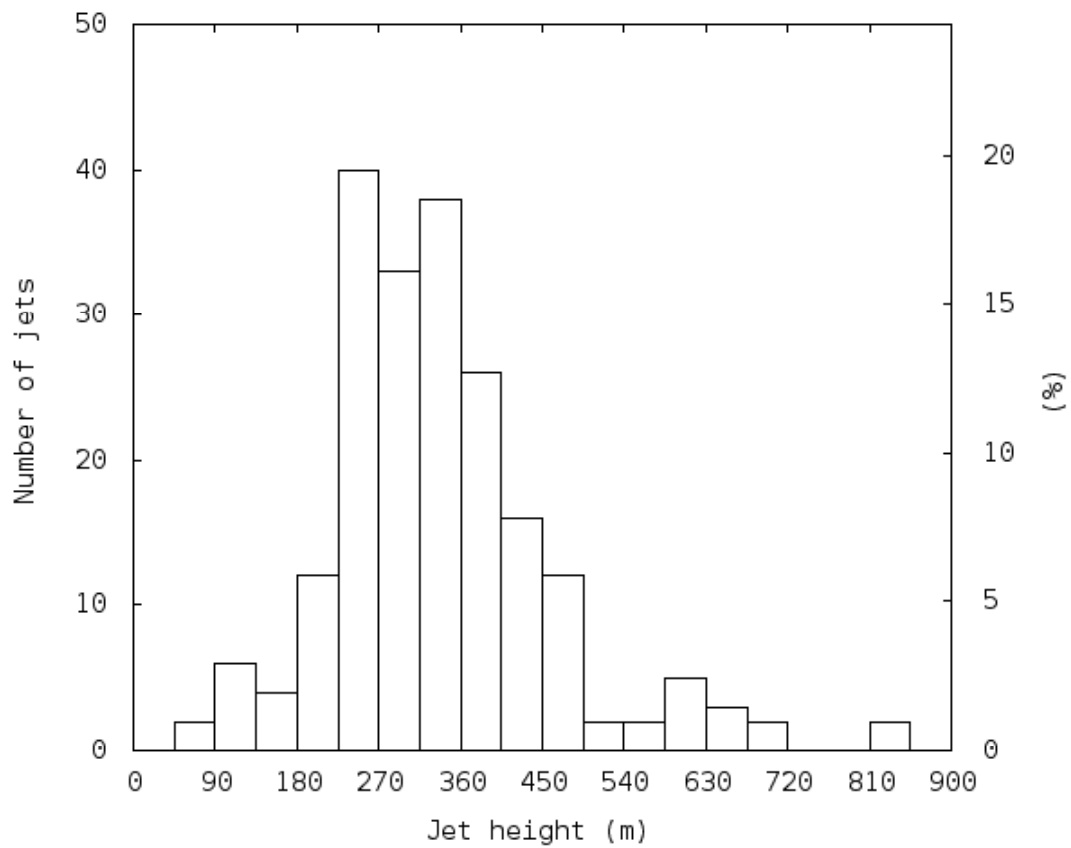


Figure 1 Histogram of jet height observed during the field campaign.

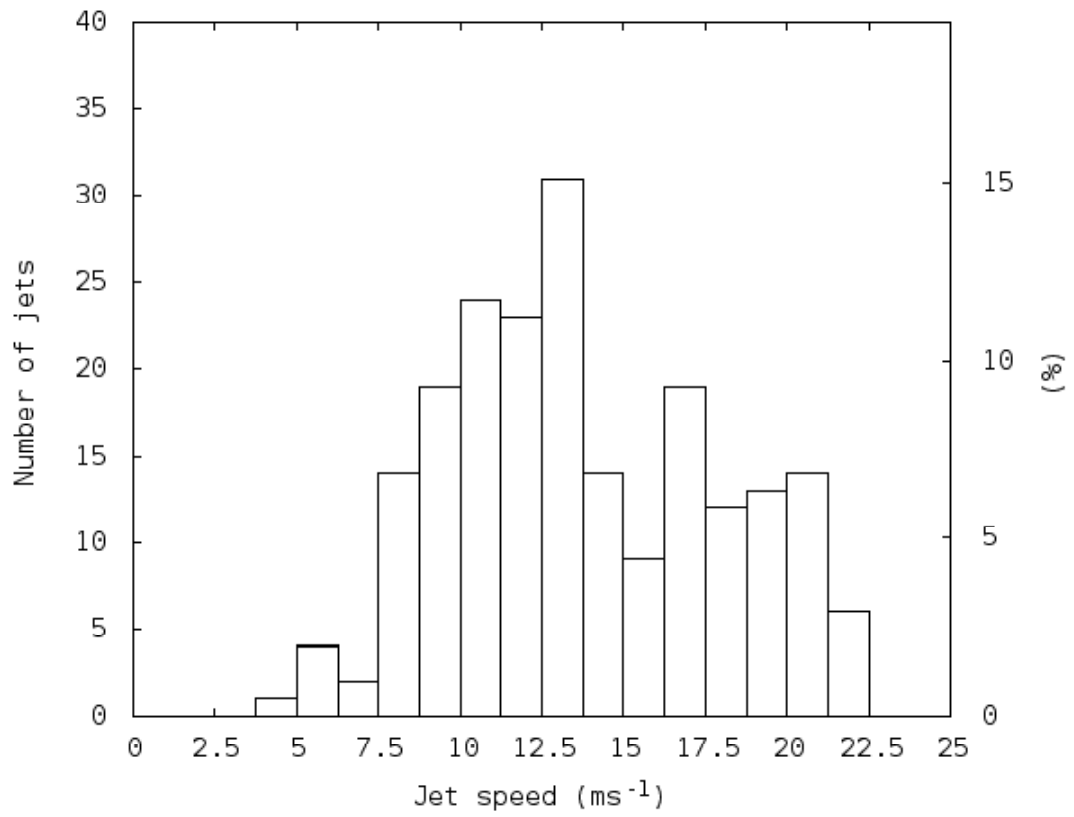


Figure 2 As in Fig. 1 but for jet speed.

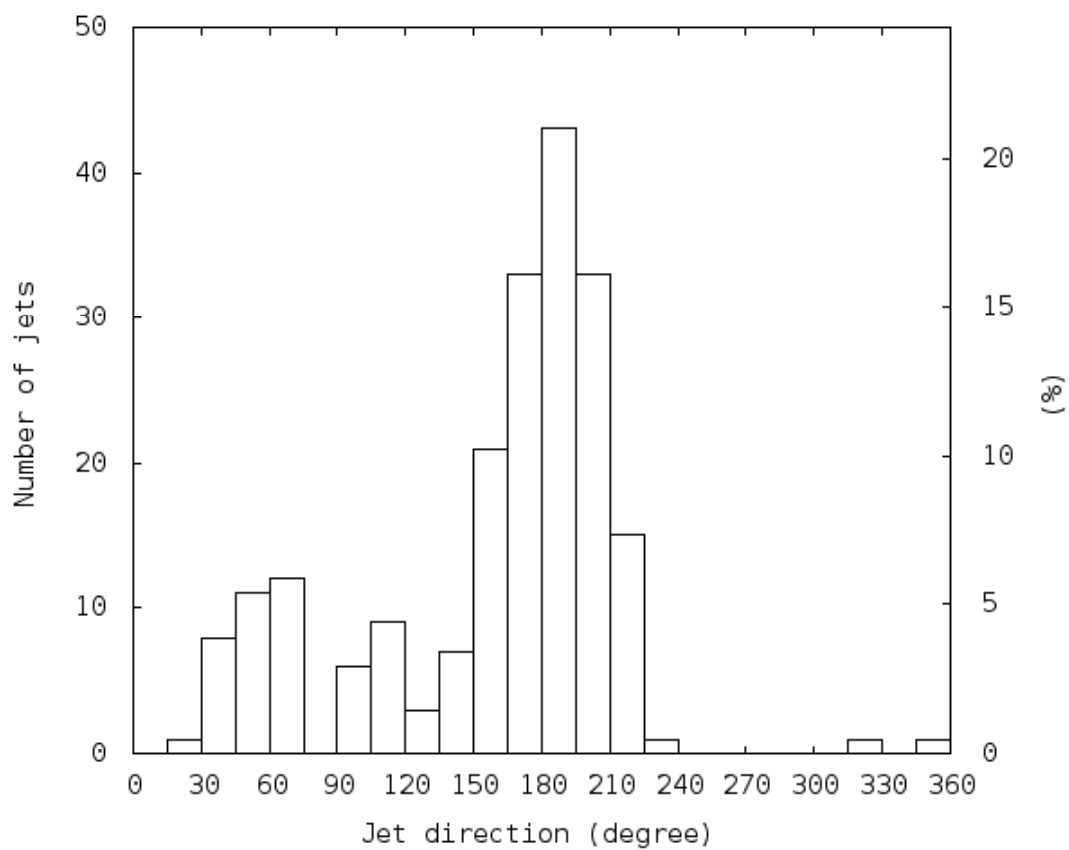


Figure 3 As in Fig. 1 but for jet direction.

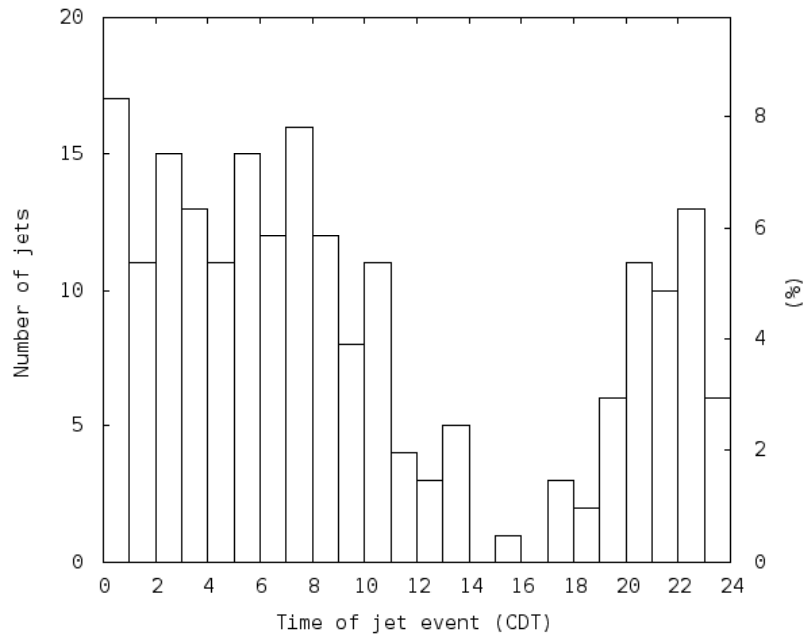


Figure 4 As in Fig. 1 but for time of occurrence.

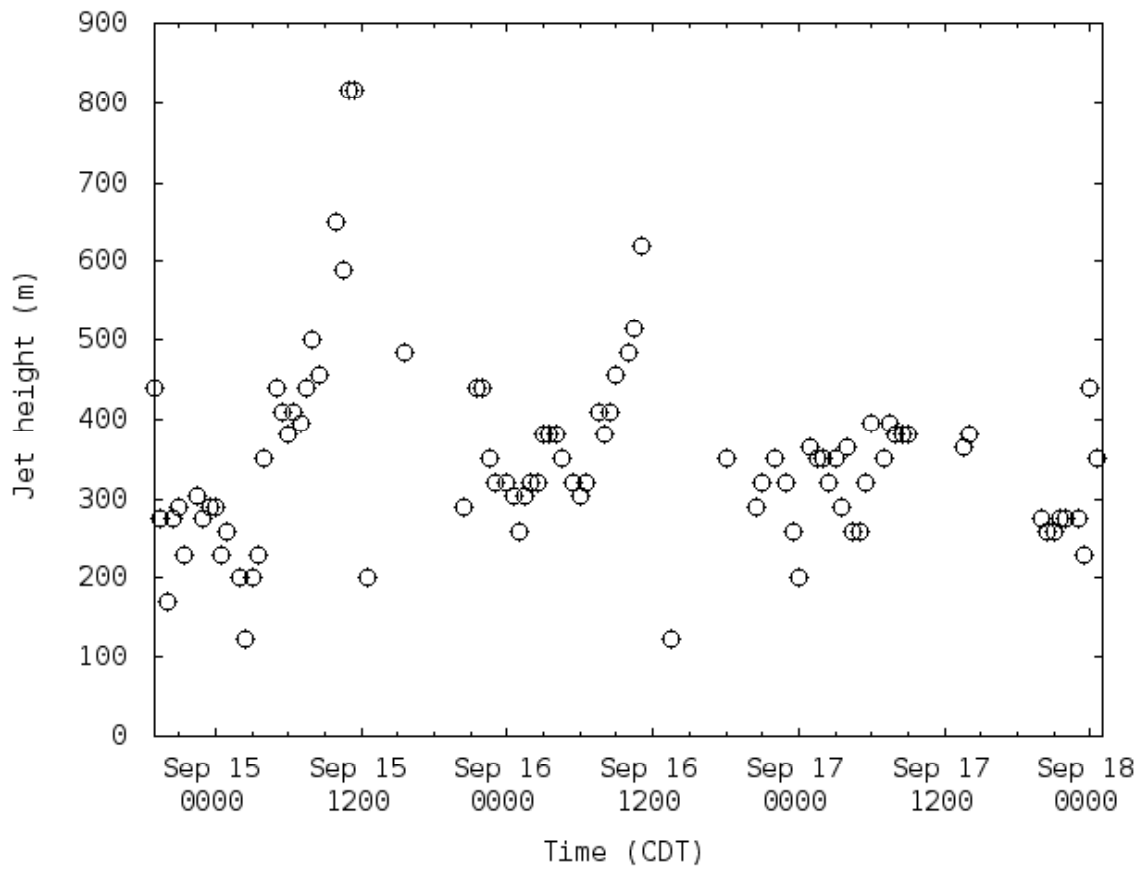


Figure 5 Time series of jet height during the period selected for simulation.

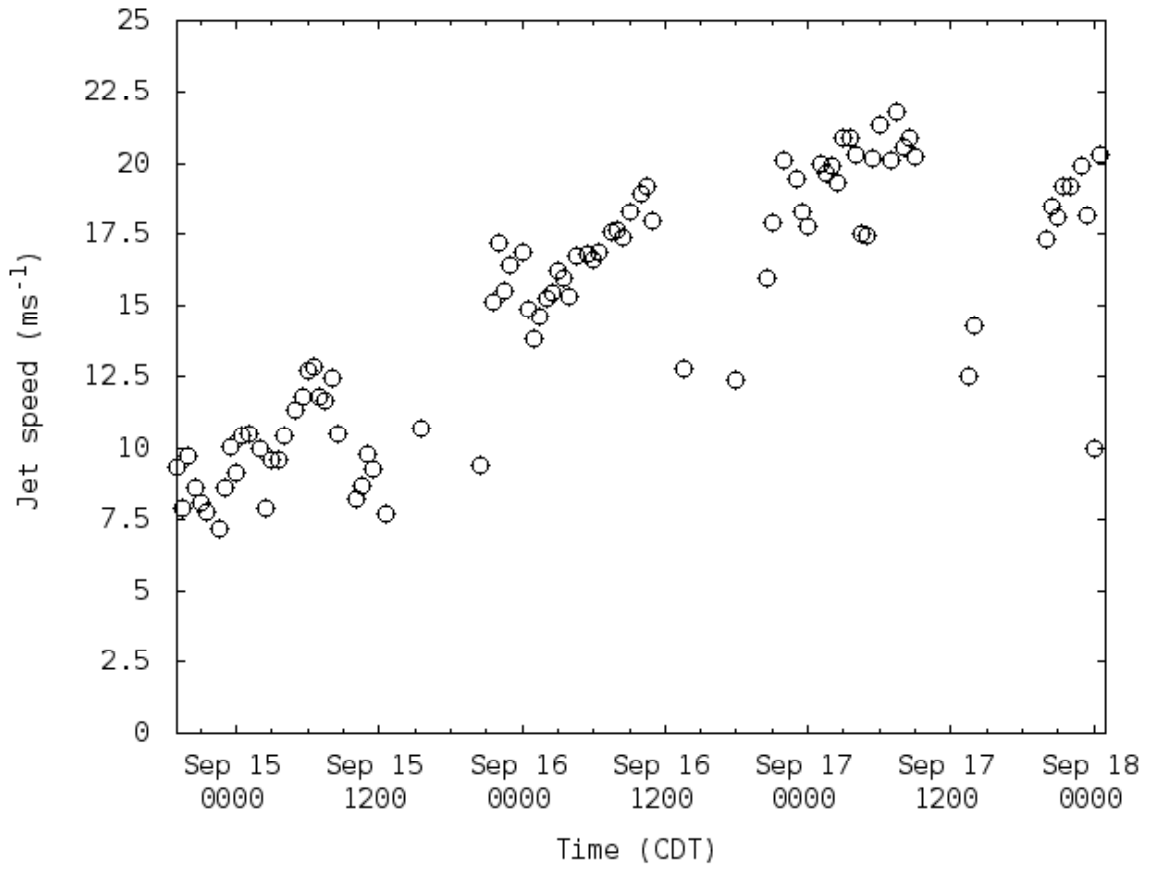


Figure 6 As in Fig. 5 but for jet speed.

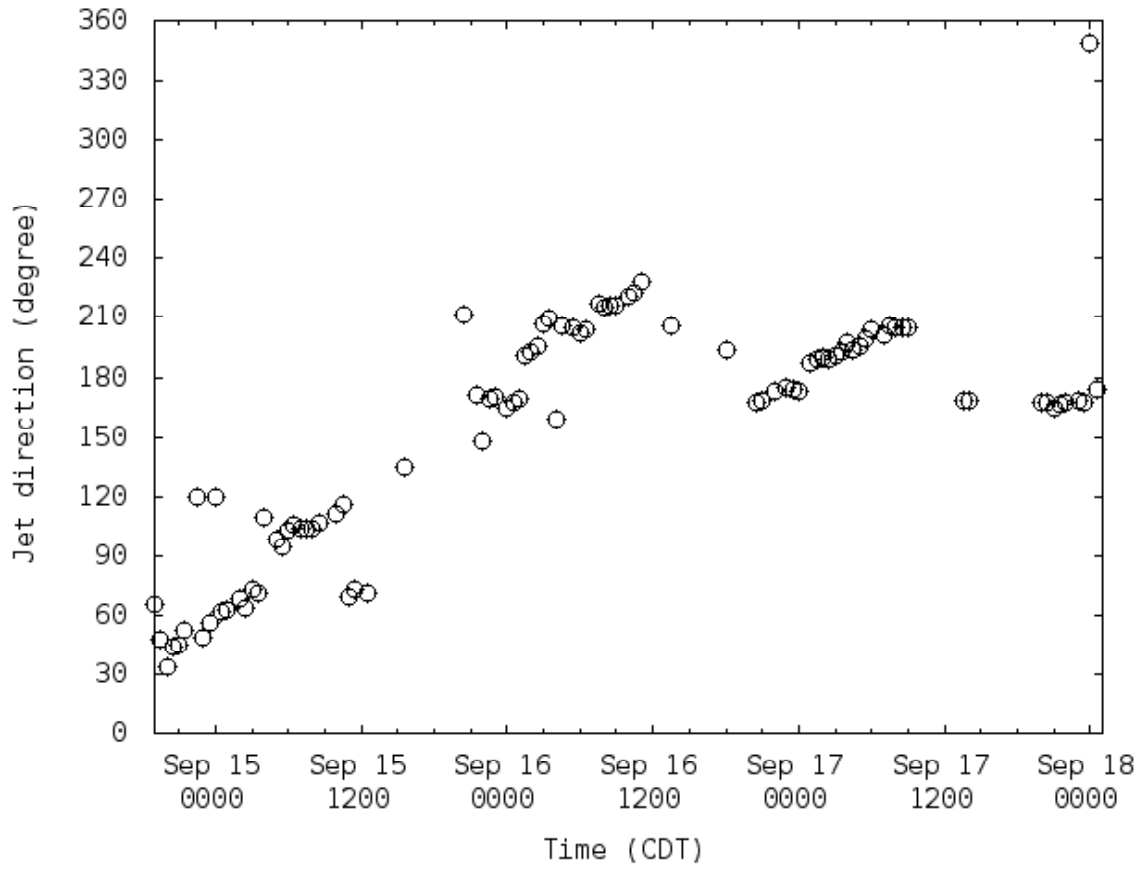


Figure 7 As in Fig. 5 but for jet direction.

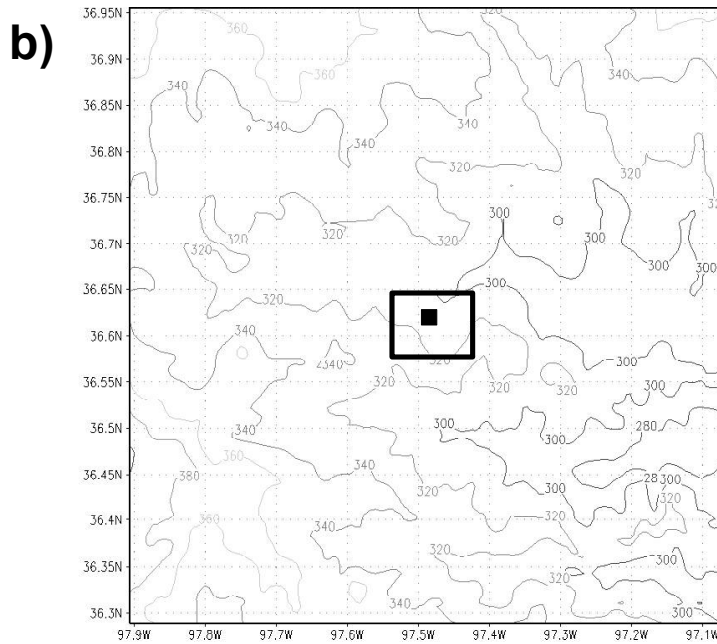
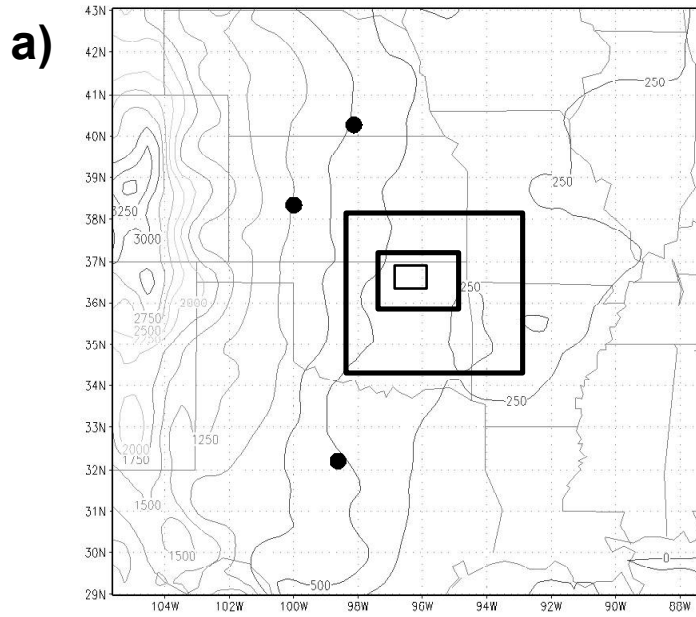


Figure 8 a) Grids 1-4 used in the RAMS simulations, along with the topography in meters. b) As in a) but for grids 4 and 5. The black square indicates the location of the ARM central Facility, where the field project was conducted. The three black dots indicate stations (Hays, KS, Hastings, NE, and Abilene, TX) used for validation.

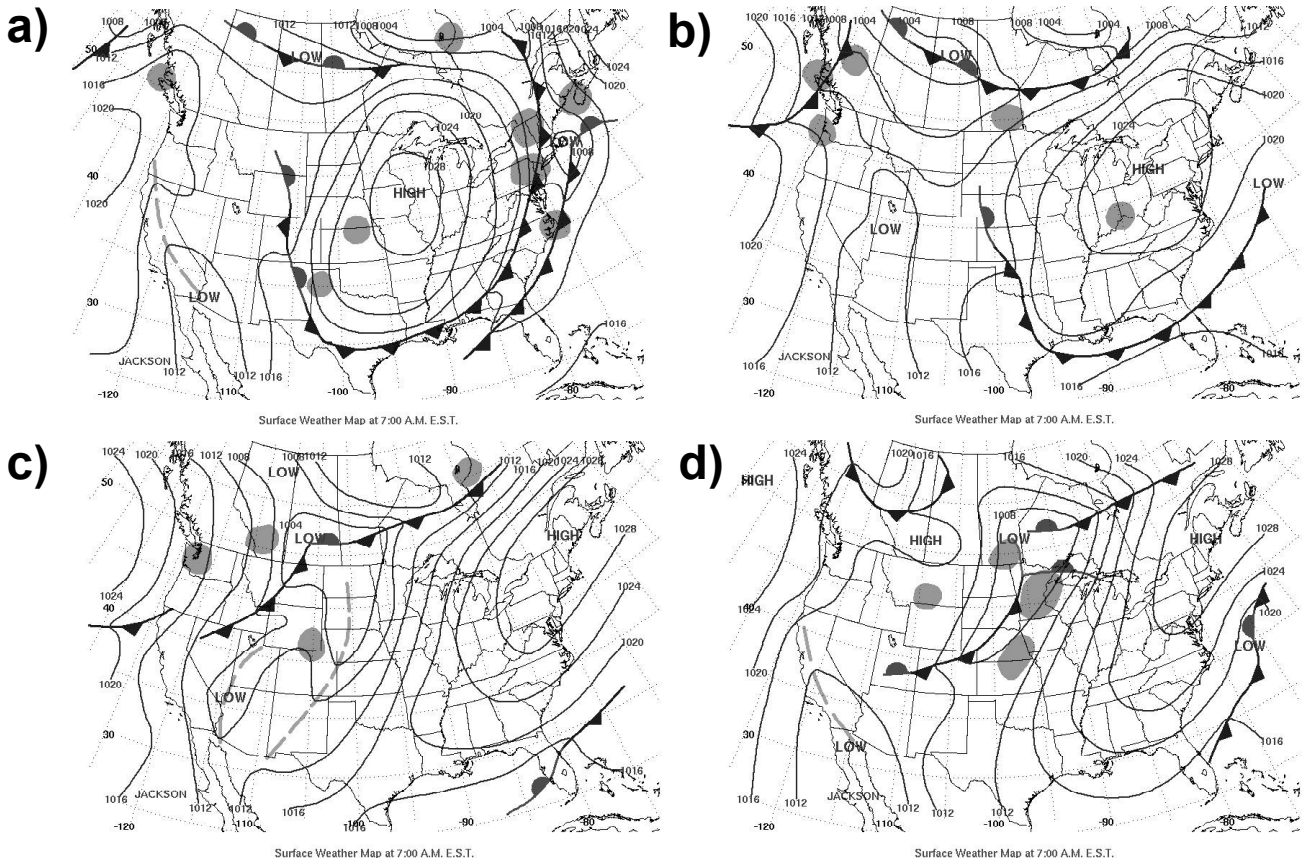


Fig. 9 Synoptic maps for a) 12Z, Sept. 15th, b) 12Z, Sept. 16th, c) 12Z, Sept. 17th, d) 12Z, Sept. 18th. Maps are from the NCEP, Hydrometeorological Prediction Center (<http://www.hpc.ncep.noaa.gov/dailywxmap/>).

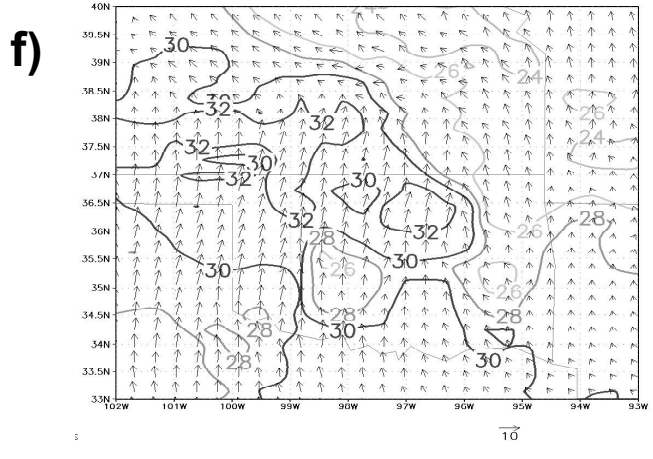
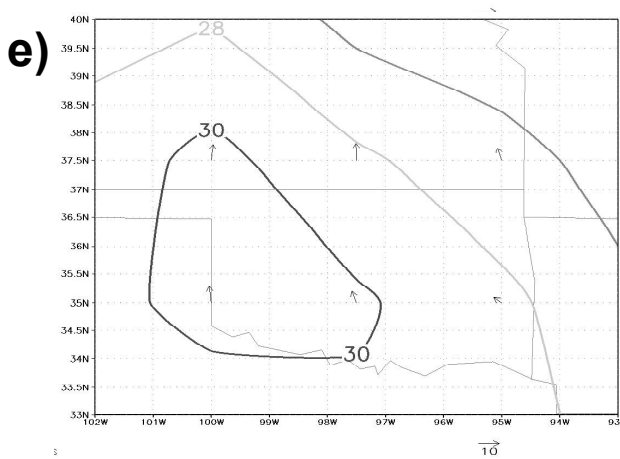
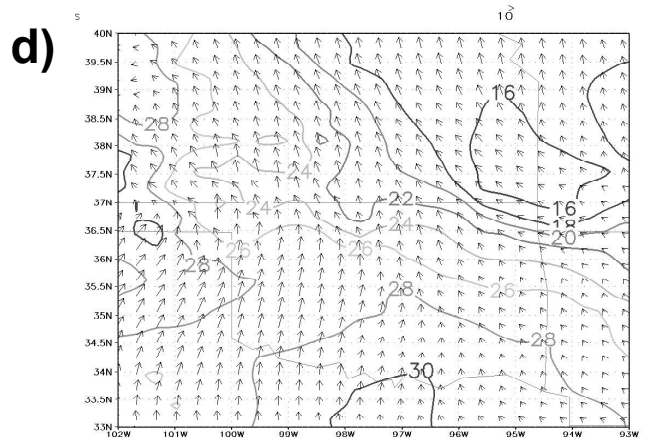
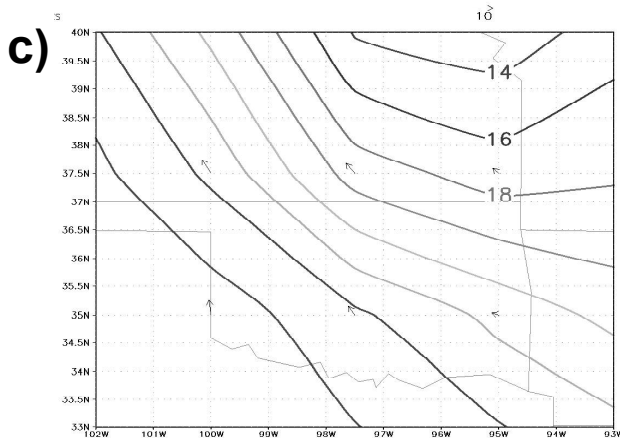
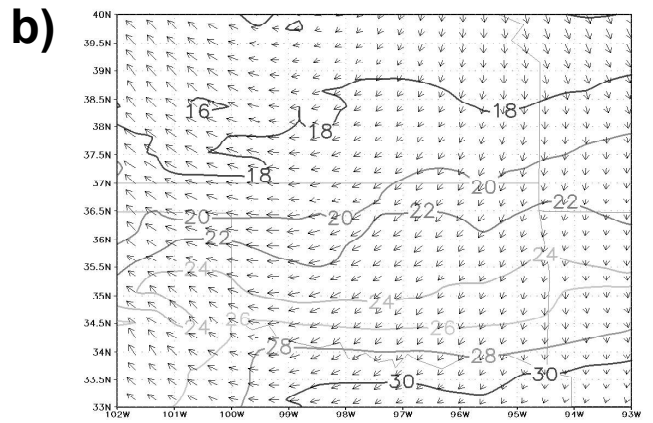
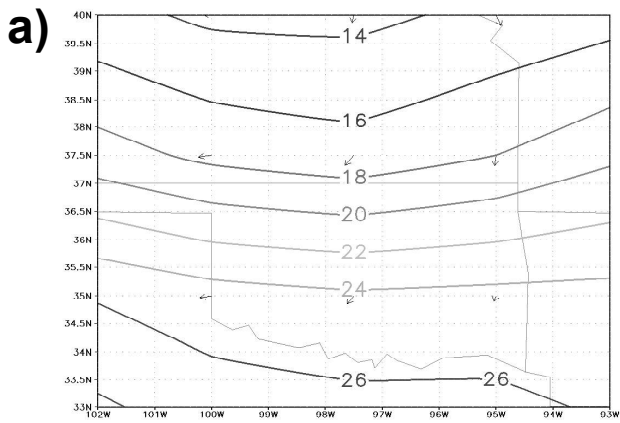


Fig. 10 Synoptic surface temperatures ($^{\circ}\text{C}$, contours) and winds (m/s , vectors) during the period from a) NCEP Reanalysis at Sept. 15, 0Z, b) RAMS at Sept. 15, 0Z, c) NCEP Reanalysis at Sept. 16, 0Z, d) RAMS at Sept. 16, 0Z, e) NCEP Reanalysis at Sept. 17, 0Z, f) RAMS at Sept. 17, 0Z

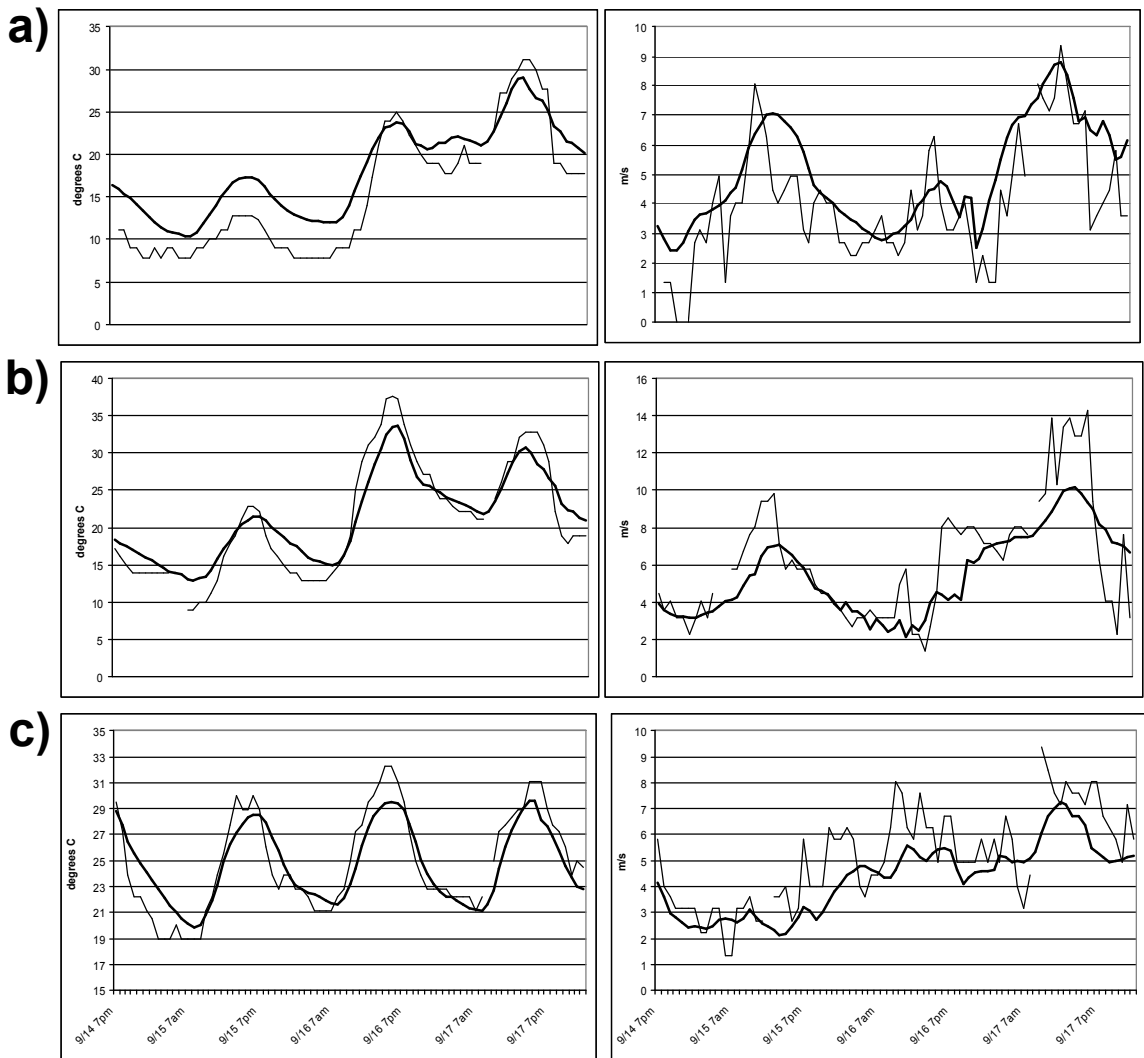


Fig. 11 RAMS grid 1 (thick line) and observed (thin line) temperature (left) and wind speed (right) at the stations (see Fig. 8) in a) Nebraska, b) Kansas, c) Texas. Observed data is from the NCDC Climate Database (<http://cdo.ncdc.noaa.gov/pls/plclimprod/poemain.accessrouter?datasetabbv=DS3505>).

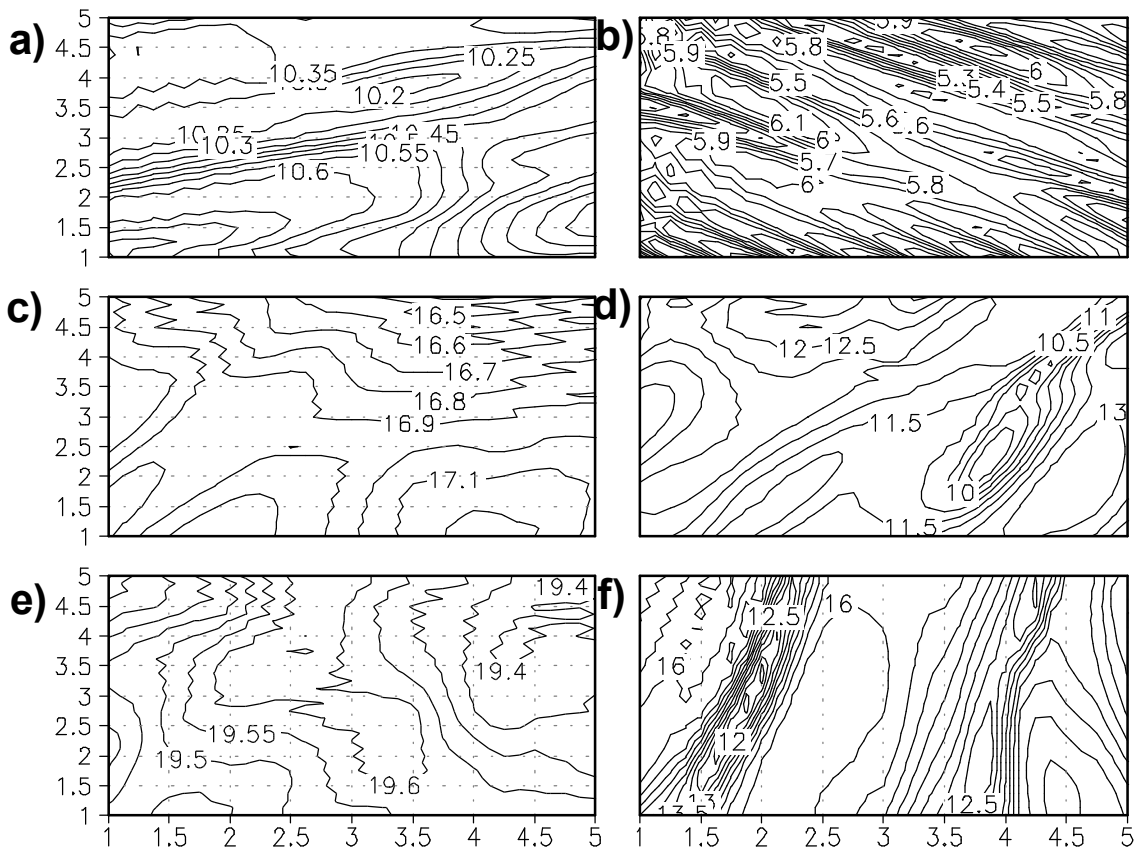
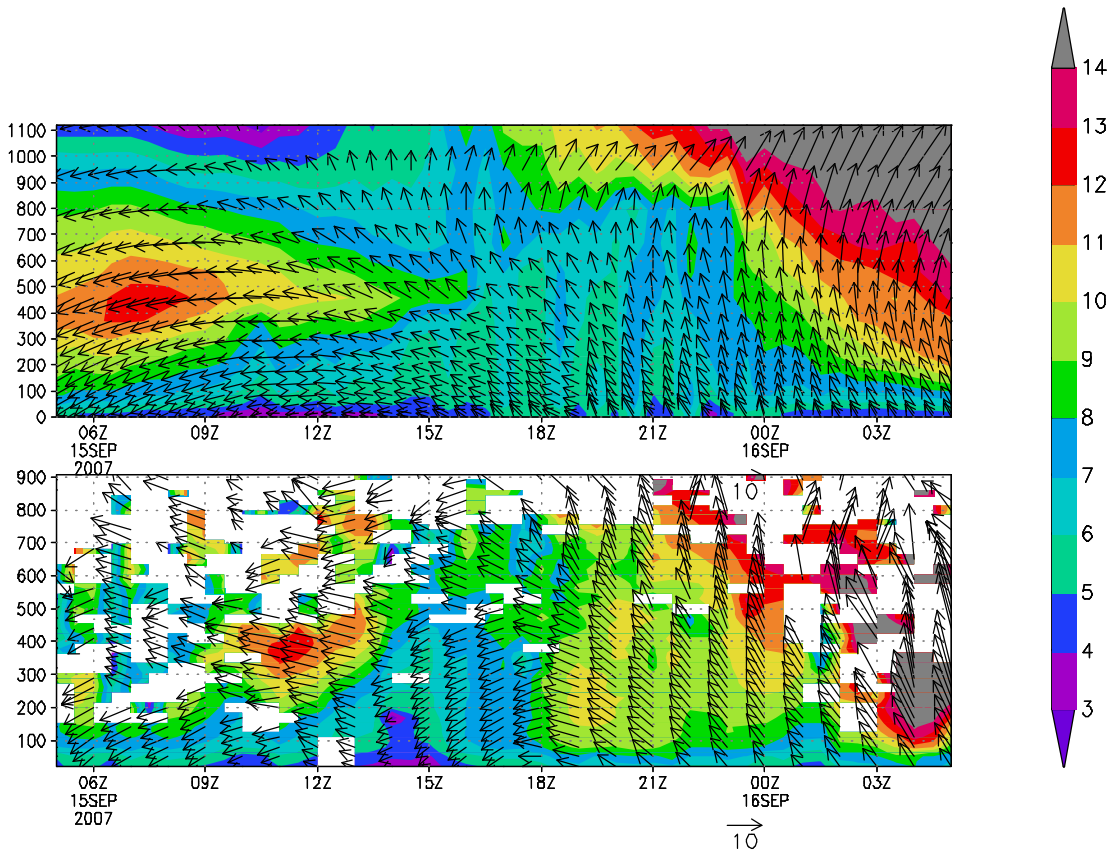


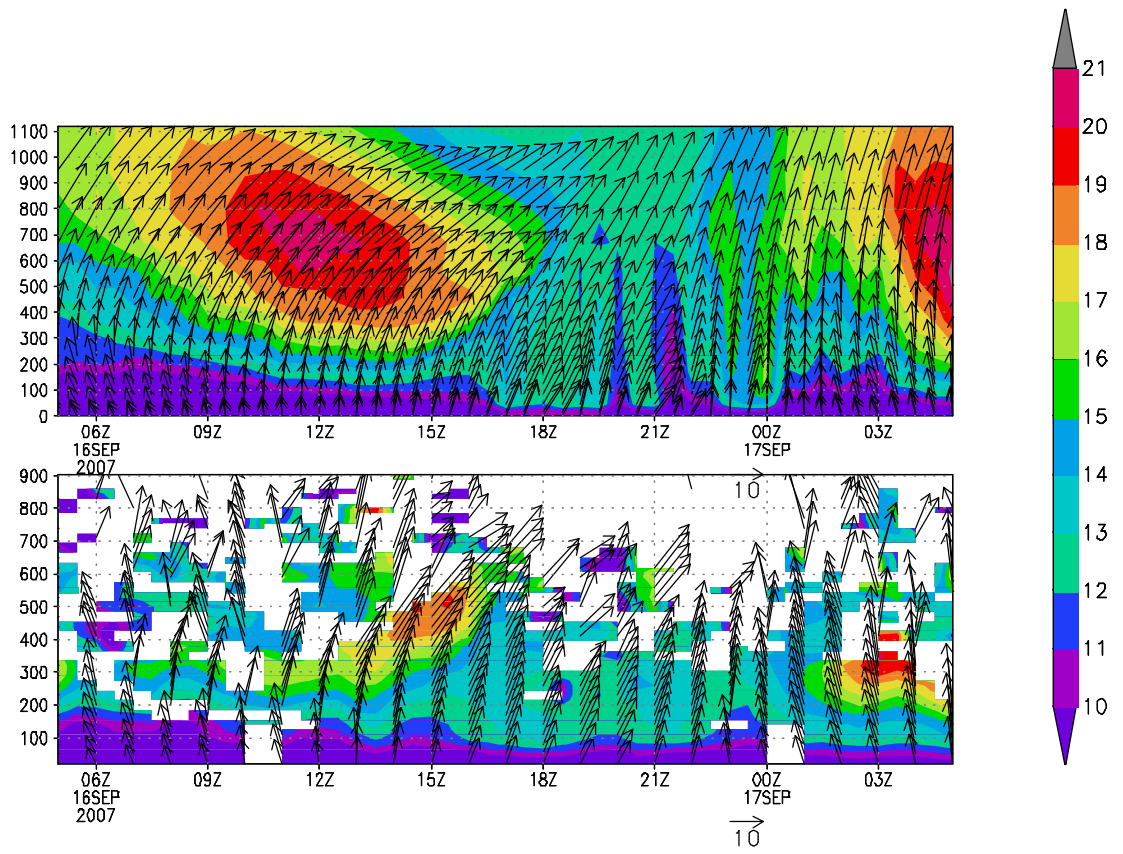
Figure 12 Horizontal wind speed (m/s) at 296m within the Grid 5 domain at a) 7Z, 9/15/07, b) 13Z, 9/16/07, c) 12Z, 9/17/07, d) 17Z, 9/15/07, e) 20Z, 9/16/07, and f) 21Z, 9/17/07. Horizontal units are in kilometers.



GrADS: COLA/IGES

2010-01-26-12:56

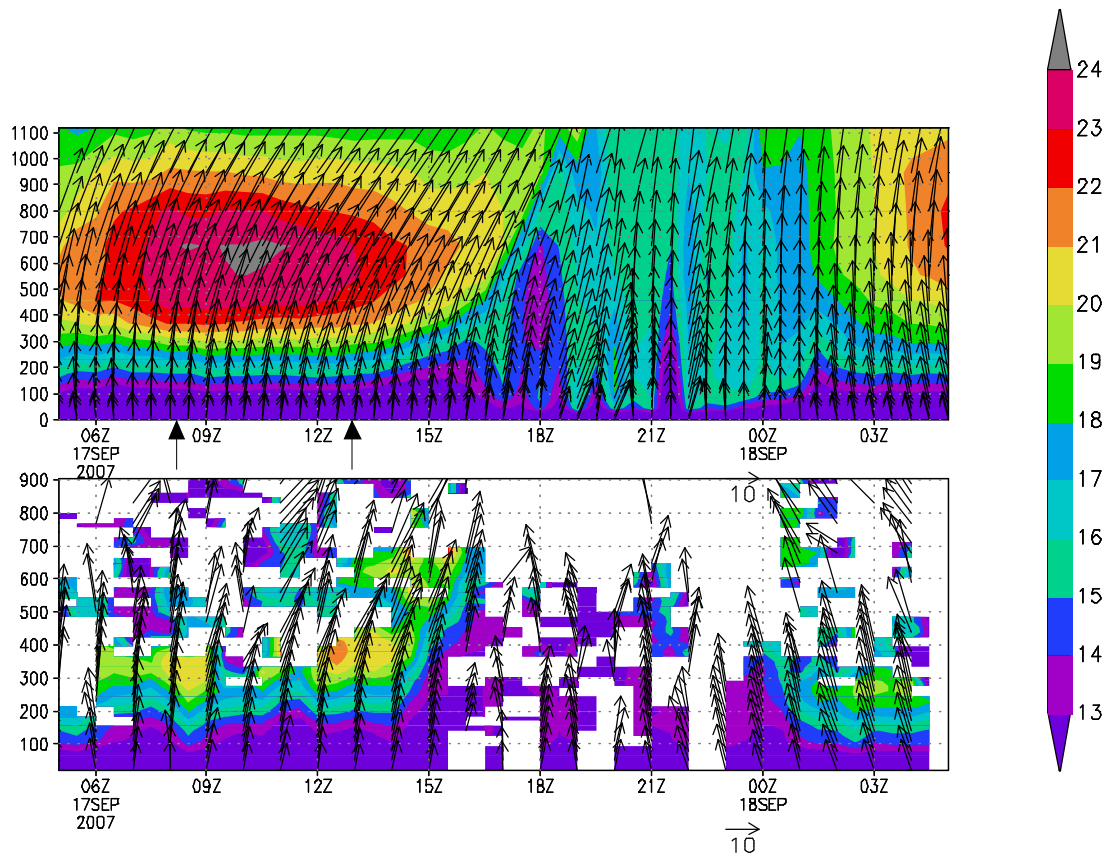
Figure 13 RAMS (top) vs. SODAR (bottom) 9/15 (midnight to midnight, CDT) wind speed (m/s, colors) and direction (arrows) as a function of height (m) at the field site.



GrADS: COLA/IGES

2010-01-26-12:56

Figure 14 As in Fig. 13 but for 9/16.



GrADS: COLA/IGES

2010-01-26-12:56

Figure 15 As in Fig. 13 but for 9/17. The black arrows indicate the nocturnal period simulated by the high-resolution model.

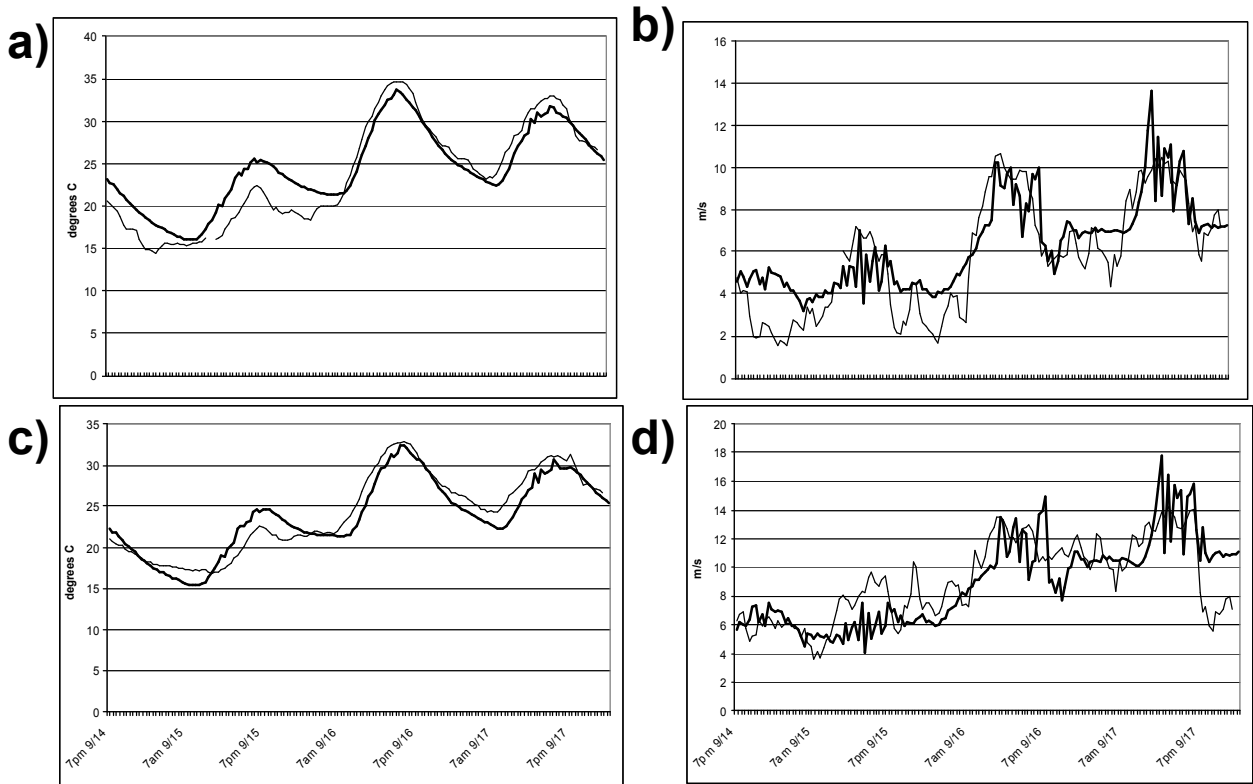


Fig. 16 a) Temperature ($^{\circ}\text{C}$) at the tower (thin line) and in the model (thick line) at 5m, b) as in a) but for 5m wind speed, c) as in a) but for temperatures at 60m, d) as in b) but for wind speeds at 60m. Both observed and model data is at 30 minute sampling.

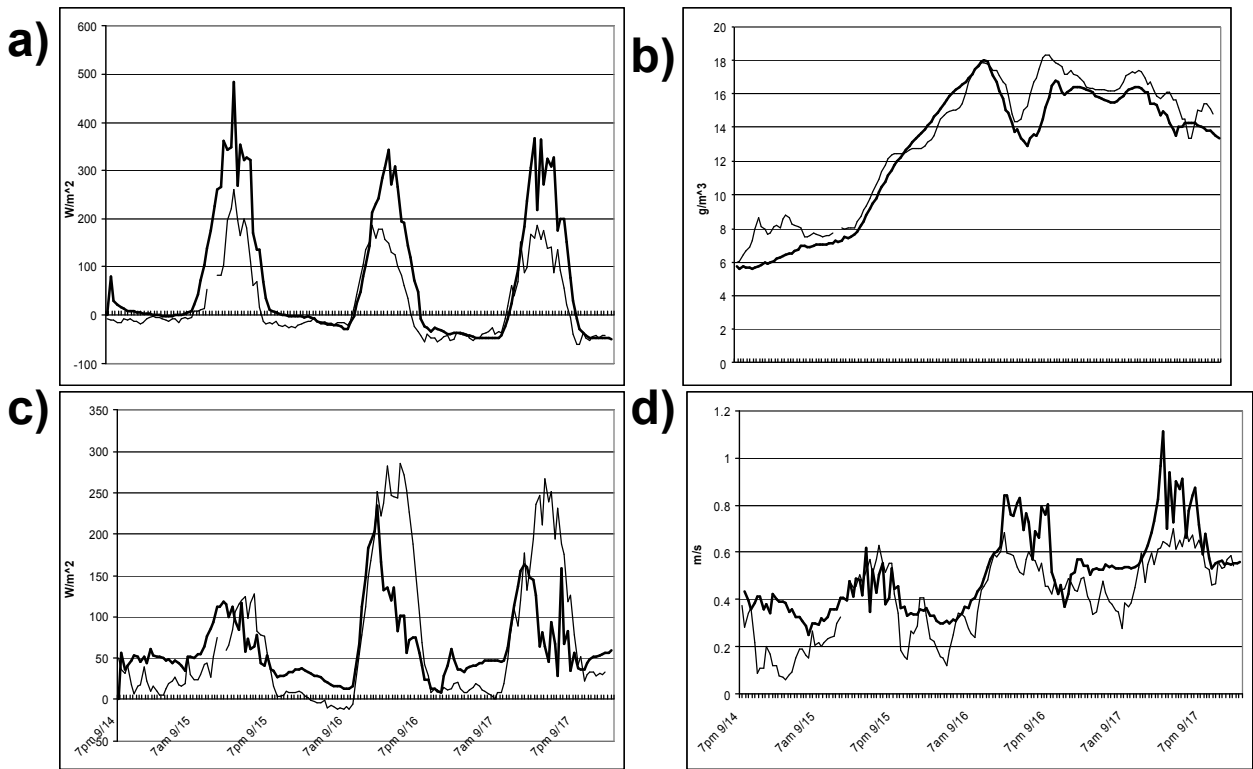


Fig. 17 RAMS simulated (thick line) and observed tower (thin line) a) sensible heat flux, b) water vapor, c) latent heat flux, and d) u^* . Both observed and model data is at 30 minute sampling.

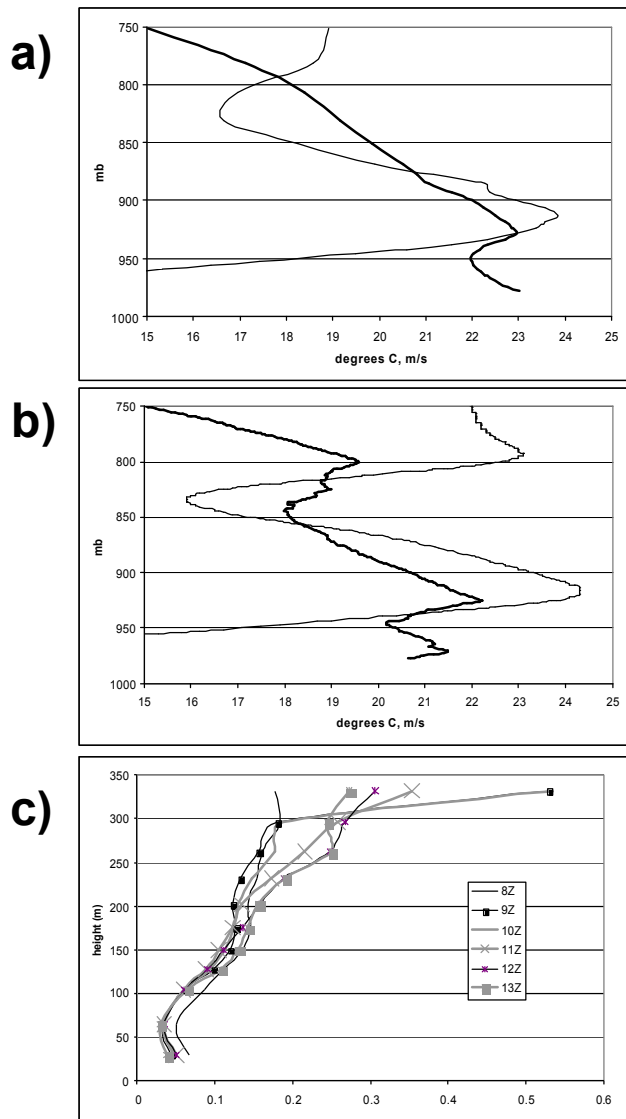


Fig. 18 a) Sounding of model temperature (thick line) and wind speed (thin line) at 12Z, Sept. 17, b) As in the top plot but for the observed sounding at the site (<http://www.arm.gov/>), c) Model Richardson number at several times during the 5.5 hour simulation period.

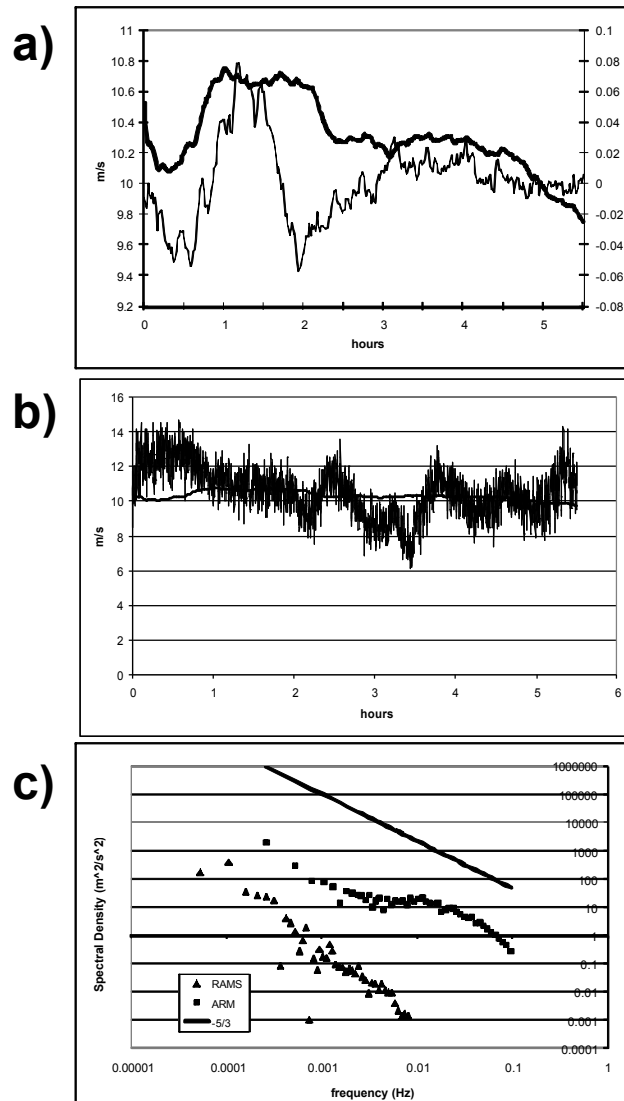


Figure 19 a) Site 60m wind speed from the Grid 6 run (thick line, left axis), along with the difference between the grid 5 and grid 6 runs (thin line, right axis). b) Observed (thin line) and simulated (thick line) 60m wind speed at the site from the 5.5 hour high resolution run. c) Power spectra of the observed and simulated 60m windspeed. The black line follows a -5/3 power law.

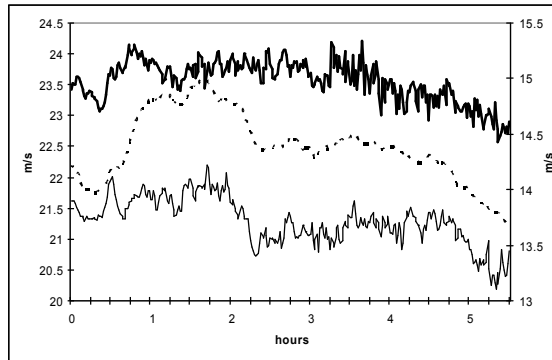


Figure 20 a) Modeled site wind speed at 550m (thick line, left axis), 350m (thin line, left axis), and 150m (dotted line).

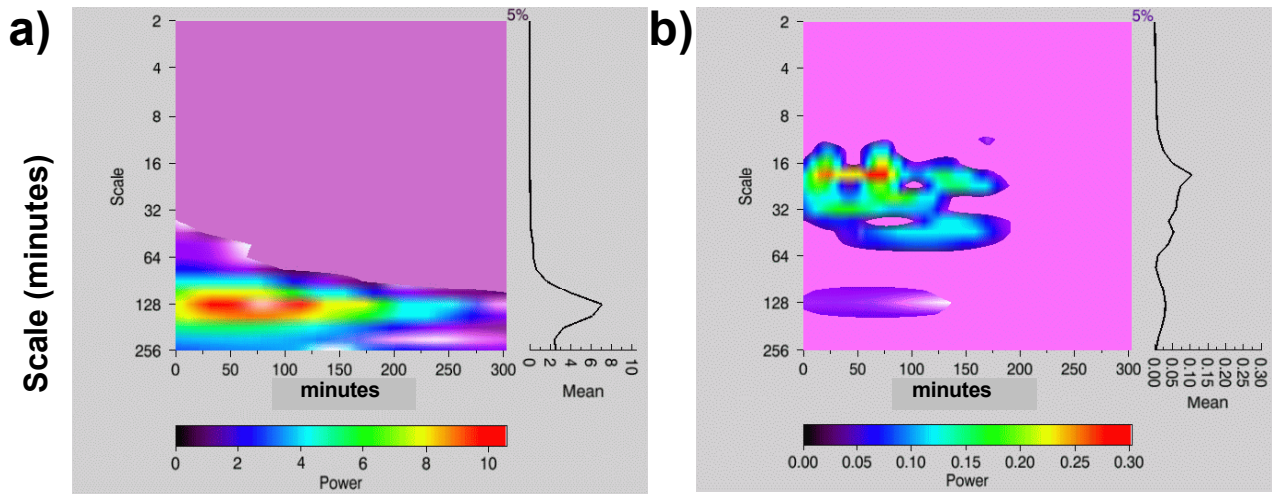


Fig. 21 Wavelet analysis of the 279m field site model windspeed for the a) LF and b) HF components. All data seen are significant at the 95% confidence level. Power units are m^2/s^2 .